UNIVERSITY OF CALIFORNIA, SAN DIEGO

Electrical signaling enables multiple modes of coordination in *B. subtilis* biofilms

A dissertation submitted in partial satisfaction of the requirements for the degree of

Doctor of Philosophy

in

Biology

by

Jacqueline Tanner Humphries

Committee in charge:

Professor Gürol Süel, Chair
Professor Jeff Hasty
Professor Justin Meyer
Professor Joseph Pogliano
Professor Emmanuel Theodorakis

2017

The Dissertation of Jacqueline Tanner Humphries is approved, and it is acceptable in quality and form for publication on microfilm and electronically:

Chair

University of California, San Diego

2017

DEDICATION

This work is dedicated to my parents who have always been my greatest supporters and to my partner who has been with me for every step of this. Thank you.

EPIGRAPH

"If a philosopher, therefore, pretends to shew us the cause of any natural effect, whether relating to matter or to mind, let us first consider whether there is sufficient evidence that the cause he assigns does really exist. If there is not, reject it with disdain, as a fiction which ought to have no place in genuine philosophy. If the cause assigned really exists, consider, in the next place, whether the effect it is brought to explain necessarily follows from it. Unless it has these two conditions, it is good for nothing."

Thomas Reid

TABLE OF CONTENTS

LIST OF FIGURES

LIST OF TABLES

ACKNOWLEDGEMENTS

Chapter 1, in full, is a reprint of the material as it appears in Liu, J., Prindle, A., Humphries, J., Gabalda-Sagarra, M., Asally, M., Lee, D-Y., Ly, S., Garcia-Ojalvo, J., and Suel, G. M., Nature, 2015. The dissertation author was a co-author of this paper.

Chapter 2, in full, is a reprint of the material as it appears in Humphries, J., Xiong, L., Liu, J., Prindle, A., Yuan, F., Arjes, H. A., Tsimring, L., and Suel, G. M., Cell, 2017. The dissertation author was the primary author of this paper.

VITA

2013 Bachelor of Arts, Scripps College

2017 Doctor of Philosophy, University of California, San Diego

PUBLICATIONS

Humphries, J., Xiong, L., Liu, J., Prindle, A., Yuan, F., Arjes, H.A., Tsimring, L., and Suel, G.M., Species-independent attraction to biofilms through electrical signaling. *Cell*. **168**, 200-209 (12 Jan 2017).

Liu, J., Prindle, A.*, Humphries, J.*, Garcia-Gabalda, M.*, Asally, M.*, Lee, D-Y., Ly, S., Garcia-Ojalvo, J., and Suel, G.M., Metabolic co-dependence gives rise to collective oscillations within biofilms. *Nature.* **523**, 550–554 (30 July 2015).

Humphries T., Humphries J., Deaf in the Time of the Cochlea. *Journal of Deaf Studies and Deaf Education.* **16(2)**, 153-63 (Spring 2011).

ABSTRACT OF THE DISSERTATION

Electrical signaling enables multiple modes of coordination in *B. subtilis* biofilms

By

Jacqueline Tanner Humphries

Doctor of Philosophy in Biology

University of California, San Diego, 2017

Professor Gürol Süel, Chair

The formation of complex multicellular bacterial communities known as biofilms is a process that requires coordination between individual cells. In this work I describe two examples of coordination in *B. subtilis* biofilms. In the first example, coordination resolves a fundamental trade-off between subpopulations within biofilms. This coordination was shown to be driven by potassium ion-channel mediated electrical signaling. In the second example, electrical signaling enables *B. subtilis* biofilms to attract motile cells from their surroundings in a species-independent manner. Attraction results in the incorporation of new members into

the pre-existing community and can give rise to mixed-species communities. These new examples of coordination in biofilms underscore the complexity of biofilm formation and provide a basis for future research.

Chapter 1 - Metabolic co-dependence gives rise to collective oscillations within biofilms

Chapter 1.1 - Abstract

Cells that reside within a community can cooperate and also compete with each other for resources. It remains unclear how these opposing interactions are resolved at the population level. Here we investigated such an internal conflict within a microbial biofilm community: Cells in the biofilm periphery not only protect interior cells from external attack, but also starve them through nutrient consumption. We discovered that this conflict between protection and starvation is resolved through emergence of long-range metabolic codependence between peripheral and interior cells. As a result, biofilm growth halts periodically, increasing nutrient availability for the sheltered interior cells. We show that this collective oscillation in biofilm growth benefits the community in the event of a chemical attack. These findings indicate that oscillations support population-level conflict resolution by coordinating competing metabolic demands in space and time, suggesting new strategies to control biofilm growth.

Chapter 1.2 – Introduction

Cooperation and competition are complex social interactions that can play critical roles in biological communities. Cooperative behavior often increases the overall fitness of the population through processes such as division of labor and production of common goods[1-4]. At the same time, individuals in a community compete with each other for limited resources, such as nutrients[5-6]. Here we investigated bacterial biofilms[7-10] to determine how the conflict between the opposing social behaviors of cooperation and competition could be resolved at the community level to increase overall fitness.

Biofilms typically form under environmental stress conditions, such as nutrient limitation[11-13]. As these bacterial communities grow larger, the supply of nutrients to interior cells becomes limited due to an increase in nutrient consumption associated with the growth of multiple layers of cells in the biofilm periphery. Severe nutrient limitation for interior cells is detrimental to the colony, since the sheltered interior cells are critical to the survival of the biofilm community in the event of an external challenge. This defines a fundamental conflict between the opposing demands for biofilm growth and maintaining the viability of protected (interior) cells (**Fig. 1.1a**). The identification of possible mechanisms that ensure the viability of the protected interior cells is fundamental to understanding biofilm development[14, 15].

In order to directly investigate how *Bacillus subtilis* biofilms continue expanding while sustaining interior cells, we converted the potentially complex three-

dimensional problem to a simpler two-dimensional scenario using microfluidics. Specifically, we used growth chambers that are unconventionally large in the lateral, x-y dimensions (3 × 3 mm), while confining biofilm thickness (z-dimension) to only a few micrometers (**Fig. 1.1b**). Therefore, biofilm expansion in this device is predominantly limited to two dimensions, creating a "pancake-like" configuration. In fact, biofilms often form in confined aqueous environments and thus this microfluidic chamber may better mimic those growth conditions[11-13]. This experimental set-up is thus ideal to interrogate how biofilms can reconcile the opposing benefits of growth and protection during biofilm development.

Chapter 1.3 - Oscillations in biofilm growth

Unexpectedly, we observed oscillations in biofilm expansion despite constant media flow within the microfluidic device (**Fig. 1.1c, d**, **and Fig. S1.1a**). Specifically, biofilms exhibit periodic reduction in colony expansion that is self-sustained and can last for more than a day (**Fig. 1.1e and Fig. S1.1b**). The period of oscillations has a mean of 2.5 ± 0.8 hours (s.d., *n* = 63 colonies), which is less than the duration of the average cell replication time of 3.4 ± 0.2 hours (s.d., *n* = 21 cell cycles) under this growth condition (**Fig. 1.1f**). Moreover, oscillations only arise when the biofilm exceeds a certain colony size. In particular, quantitative measurements obtained from 53 individual biofilms indicate that oscillations emerge in colonies that exceed an average diameter of 580 ± 85 μm (s.d., *n* = 53 colonies), which corresponds to approximately

one million cells (**Fig. 1.1g, h**). Together, these data show that oscillations arise during biofilm formation and are self-sustained.

Given that biofilms typically form under nutrient limited conditions and bacterial growth is generally controlled by metabolism, we hypothesized that metabolic limitation plays a key role in the observed periodic halting of biofilm expansion. In particular, after determining that carbon source limitation did not play an essential role in the oscillations (**Fig. S1.2**), we focused on nitrogen limitation. The standard biofilm growth media (MSgg, see **Methods: Growth conditions**) used to study *B. subtilis* biofilm development contains glutamate as the only nitrogen source[16]. In most organisms including *B. subtilis*, glutamate is combined with ammonium by glutamine synthetase (GS) to produce glutamine, which is essential for biomass production and growth (**Fig. 1.2a**)[17]. Cells can obtain the necessary ammonium from glutamate through the enzymatic activity of glutamate dehydrogenase (GDH), expressed by the *rocG* or *gudB* genes in the undomesticated *B. subtilis* used in this study (**Fig. 1.2a**)[18-20]. To determine whether biofilms experience glutamine limitation, we measured expression of *nasA*, one of several genes activated in response to a lack of glutamine[21]. Results show that biofilms indeed experience glutamine limitation during growth. Specifically, supplementation of growth media directly with glutamine reduced *nasA* promoter expression, but did not affect expression of a constitutive promoter, confirming glutamine limitation within the biofilm (**Fig. 1.2b**). More strikingly, addition of exogenous glutamine eliminated periodic halting of biofilm

growth (**Fig. 1.2c and Fig. S1.3a**). These findings suggest that glutamine limitation plays a critical role in the observed oscillations during biofilm expansion.

The synthesis of glutamine requires both glutamate and ammonium, therefore we investigated which of these substrates could be responsible for the observed glutamine limitation. Glutamate is provided in the media and is thus readily available to cells in the periphery of the biofilm. On the other hand, consumption of glutamate by peripheral cells is likely to limit its availability to cells in the biofilm interior (**Fig. 1.2d**). One may thus expect that oscillations in biofilm expansion could be due to periodic pausing of cell growth in the biofilm interior. Accordingly, we set out to establish whether interior or peripheral cells exhibited changes in growth. By tracking physical movement within the biofilm, we uncovered that only peripheral cells grow, and that oscillations in biofilm expansion therefore arise exclusively from periodic halting of peripheral cell growth (**Fig. 1.2e, Fig. S1.4a**). This finding was further confirmed by single cell resolution analysis that directly showed periodic reduction in the growth of peripheral cells (**Fig. S1.4b**). This surprising pausing of cell growth in the periphery, despite unrestricted access to glutamate, suggests that glutamate cannot be the limiting substrate for glutamine synthesis. Consistent with this expectation, biofilm oscillations were not quenched by supplementation of the media with glutamate (**Fig. 1.2f**). Therefore, it is not glutamate, but ammonium that appears to be the limiting substrate for glutamine synthesis in the biofilm periphery.

Since cells can self-produce ammonium from glutamate, we next sought to determine how peripheral cells could experience periodic ammonium limitation despite a constant supply of glutamate in the media. It is well known that ammonium production is a highly regulated process that is dependent on the metabolic state of the cell and the ambient level of ammonium in the environment[22]. In particular, since ammonium is in equilibrium with ammonia vapor, which can freely cross the cell membrane and be lost to the extracellular media[23], the production of ammonium is known as a "futile cycle". Cells therefore preferentially use extracellular (ambient) ammonium for growth, rather than producing their own[24-26]. Since peripheral cells are exposed to media flow, they are particularly susceptible to this futile cycle of ammonia loss. In this sense, since ammonium is not provided in the media, even if all cells produce ammonium, the biofilm interior will be the major source for ambient ammonium (**Fig. 1.2d**). Consequently, the simplifying hypothesis is that growth of peripheral cells relies on ammonium produced within the biofilm. To test this conjecture, we supplemented the media with 1 mM ammonium, which eliminated the periodic halting in biofilm expansion (**Fig. 1.2g and Fig. S1.3b and S1.5a**). When additional ammonium was suddenly removed from the media, growth in the biofilm periphery halted as expected (**Fig. S1.5b**). These findings indicate that peripheral cells preferentially rely on extracellular ammonium produced within the biofilm for their growth.

Chapter 1.4 - Metabolic codependence between the biofilm periphery and interior

The results described above evoke the intriguing possibility that ammonium limitation for peripheral cells may arise due to glutamate limitation for interior cells. Specifically, persistent consumption of glutamate by peripheral cells can deprive the interior cells of the necessary glutamate for ammonium production. In order to explore this nontrivial hypothesis, we turned to mathematical modeling to develop a conceptual framework and generate experimentally testable predictions. Our model describes separately the metabolic dynamics of interior and peripheral cells and the metabolite exchange between them, where the distinction of the two subpopulations depends on nutrient availability (see **Methods**). The model thus consists of two main assumptions (**Fig. 1.3a**): First, consumption of glutamate during growth of peripheral cells deprives interior cells of this nutrient and thus inhibits ammonium production in the biofilm interior. Second, the growth of peripheral cells depends predominantly on ammonium that is produced by metabolically stressed interior cells. A model based on these two simplifying assumptions (**Fig. 1.3b**) generates oscillations consistent with our experimental observations (**Fig. 1.3c-e**) and reproduces the effects of supplementing the media with glutamine, glutamate and ammonium (**Fig. 1.3f-h, Fig. S1.6 and Methods**). The model also accounts for the observed slight increase of the oscillation period by considering an increase in the ratio of interior to peripheral cells over time (**Fig. S1.1b and S1.6f**). Therefore, this simple model shows that periodic halting in biofilm growth can result from metabolic codependence between cells in the

biofilm periphery and interior that is driven by glutamate consumption and ammonium production, respectively.

The metabolic codependence between interior and peripheral cells gives rise to the surprising prediction that external attack could promote growth within the biofilm. Specifically, killing of peripheral cells will eliminate their glutamate consumption, which will increase glutamate availability in the biofilm and thereby promote growth of interior cells (**Fig. 1.4a**). To test this hypothesis, we measured cell death and growth within oscillating biofilms (**Fig. 1.4b, top and Fig. S1.7**). When we exposed the biofilm to media containing hydrogen peroxide (H_2O_2), we observed increased cell death predominantly in the biofilm periphery (**Fig. 1.4b, bottom and Fig. S1.8**). As predicted, death of peripheral cells led to growth of interior cells (**Fig. 1.4c and Fig. S1.8**). To verify that this response is not uniquely triggered by H_2O_2, we exposed biofilms to the antibiotic chloramphenicol and again observed growth of interior cells (**Fig. S1.8**). These findings further support our hypothesis that glutamate consumption by peripheral cells limits its availability in the biofilm.

Chapter 1.5 - The benefit of biofilm oscillations

Our model also assumes that glutamate starvation of the biofilm interior reduces the production of ammonium that can support peripheral cell growth. This assumption provokes the question as to why peripheral cells do not simply overcome their dependence on extracellular ammonium by increasing intracellular production[27,

[28]. To address this question, we constructed a strain that contains an inducible copy of the GDH gene *rocG* (**Fig. 1.4d**). We confirmed that GDH overexpression was not toxic to individual cells and did not affect their growth rate (**Fig. S1.9**). In contrast, the induction of GDH expression in the biofilm quenched growth oscillations (**Fig. 1.4e and Fig. S1.3c**) and resulted in high levels of cell death in the colony interior (**Fig. 1.4f, top**). This result explains why peripheral cells do not appear to utilize the simple strategy of overcoming their dependence on extracellular ammonium: such a strategy would result in the continuous growth of peripheral cells, starving and ultimately causing the death of sheltered interior cells within the biofilm. Periodic halting of peripheral cell growth due to extracellular ammonium limitation thus promotes the overall viability of the biofilm.

The ability of the biofilm to regenerate itself in the event of an external attack suggested that killing the biofilm interior first would be a more effective strategy for biofilm extermination. Accordingly, we exposed the GDH overexpression strain to hydrogen peroxide and again measured growth and death. As described above, GDH induction causes death of interior cells. Exposing the GDH overexpression strain to hydrogen peroxide resulted in more effective global killing throughout the biofilm (**Fig. 1.4f, g, bottom**). While in the wild-type biofilm interior cells begin to grow in response to an external attack, metabolic independence between interior and peripheral cells in the GDH strain interferes with this defense mechanism (**Fig. 1.4h**). This outcome is also consistent with modeling predictions (**Fig. 1.4h, inset**). Oscillations in biofilm

growth that are driven by metabolic codependence thus promote the resilience of the biofilm community by sustaining the viability of the sheltered interior cells that are most likely to survive in the event of an environmental stress (**Fig. 1.4i**).

Chapter 1.6 – Discussion

The data presented here reveal that intracellular metabolic activity within biofilms is organized in space and time, giving rise to codependence between interior and peripheral cells. Even though bacteria are single-celled organisms, the metabolic dynamics of individual cells can thus be regulated in the context of the community. This metabolic codependence can in turn give rise to collective oscillations that emerge during biofilm formation and promote the resilience of biofilms against chemical attack. The community-level oscillations also support the ability of biofilms to reach large sizes, while retaining a viable population of interior cells. Specifically, periodic halting of peripheral cell growth prevents complete starvation and death of the interior cells. This overcomes the colony size limitation for a viable biofilm interior that would otherwise be imposed by nutrient consumption in the biofilm periphery. Metabolic codependence in biofilms therefore offers an elegant solution that resolves the social conflict between cooperation (protection) and competition (starvation) through oscillations.

The intriguing discovery of biofilm oscillations presented here also provokes new questions. While cellular processes such as swarming or expression of

extracellular matrix components are not required for the observed biofilm oscillations (**Fig. S1.10**), it will be interesting to pursue whether such cellular processes are influenced by oscillatory dynamics[29]. Another question worth pursuing is whether metabolic codependence can also arise in other biofilm-forming species. Perhaps other metabolic branches where metabolites can be shared among cells could also give rise to oscillations in biofilm growth. It will be exciting to pursue these questions in future studies to obtain a better understanding of biofilm development.

Our observations also suggest future strategies to cope with the intriguing resilience of biofilms in the face of environmental stresses, such as antibiotic exposure. In particular, our findings show that straightforward application of stress (such as H_2O_2 or chloramphenicol) to the biofilm counterintuitively promotes growth, effectively rejuvenating the biofilm. Death of the colony periphery relieves the repression on the growth of interior cells, allowing them to regenerate a new biofilm periphery and interior. In contrast, manipulation of the metabolic codependence may yield a more effective approach to control biofilm formation. Specifically, promoting continuous growth of peripheral cells can starve the biofilm interior, leaving behind the exposed peripheral cells that can more easily be targeted by external killing factors. Therefore, the metabolically driven collective oscillations in biofilm expansion described here not only reveal fundamental insights into the principles that govern formation of multicellular communities, but also suggest new strategies for manipulating the growth of biofilms.

Chapter 1.7 - Figures

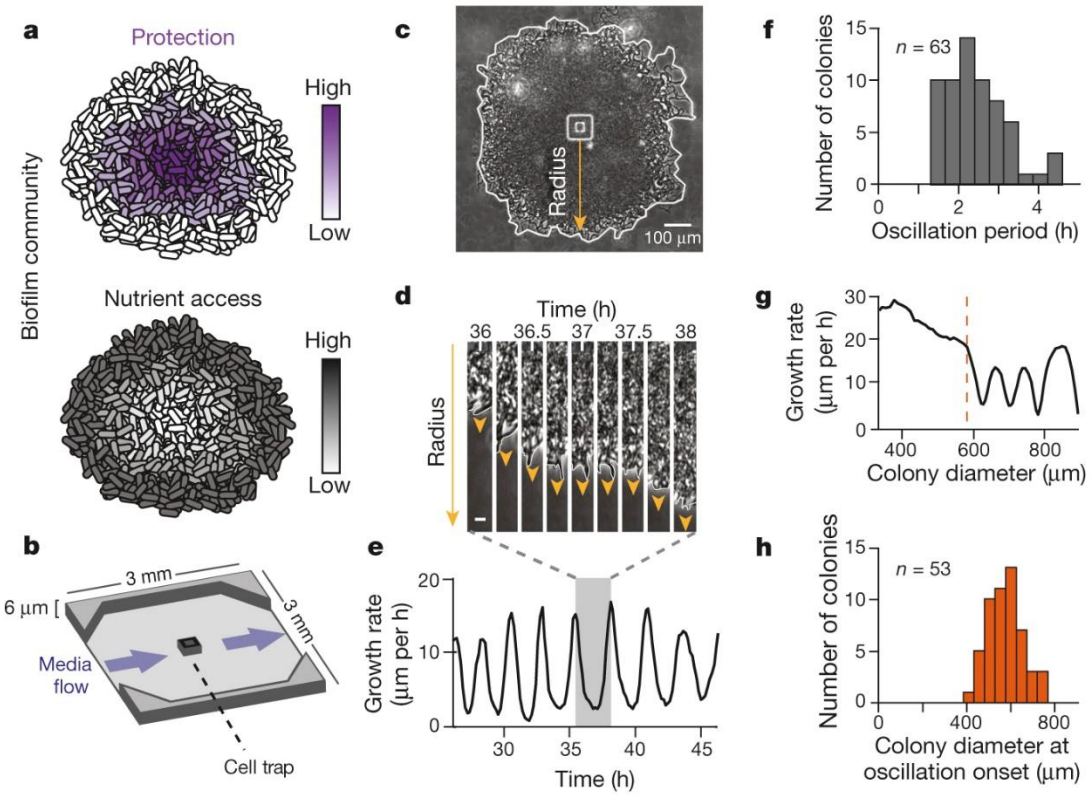

Figure 1.1. Biofilms grown in microfluidic devices show oscillations in colony expansion. **a,** Biofilms must reconcile opposing demands for protection from external challenges (gradient indicated in purple) and access to nutrients (gradient indicated in gray). **b,** Schematic of the microfluidic device used throughout this study. Direction of media flow is indicated by the blue arrows. **c,** Phase contrast image of a biofilm growing in the microfluidic device. The yellow arrow indicates the region of interest in panel (**d**). **d,** Filmstrip of a radius of the biofilm over time shows a pause in colony expansion. This film strip represents one cycle of biofilm oscillations, indicated by the shaded region in panel *e*. Scale indicates 5 µm. **e,** Growth rate over time shows persistent oscillations in colony expansion. **f,** Histogram of the average period of oscillations for each colony (*n* = 63 colonies, mean = 2.5 hours, s.d. = 0.8 hours). The cell replication time is approximately 3.4 hours under these conditions (Methods: Data Analysis). **g.** Growth rate as a function of colony diameter (which increases in time) shows that early colony growth does not exhibit oscillations. The orange line indicates the diameter (~600 µm) at which this colony initiates oscillations. **h,** Histogram of the diameter at which a colony begins to oscillate (*n* = 53 colonies, mean = 576 µm, s.d. = 85 µm).

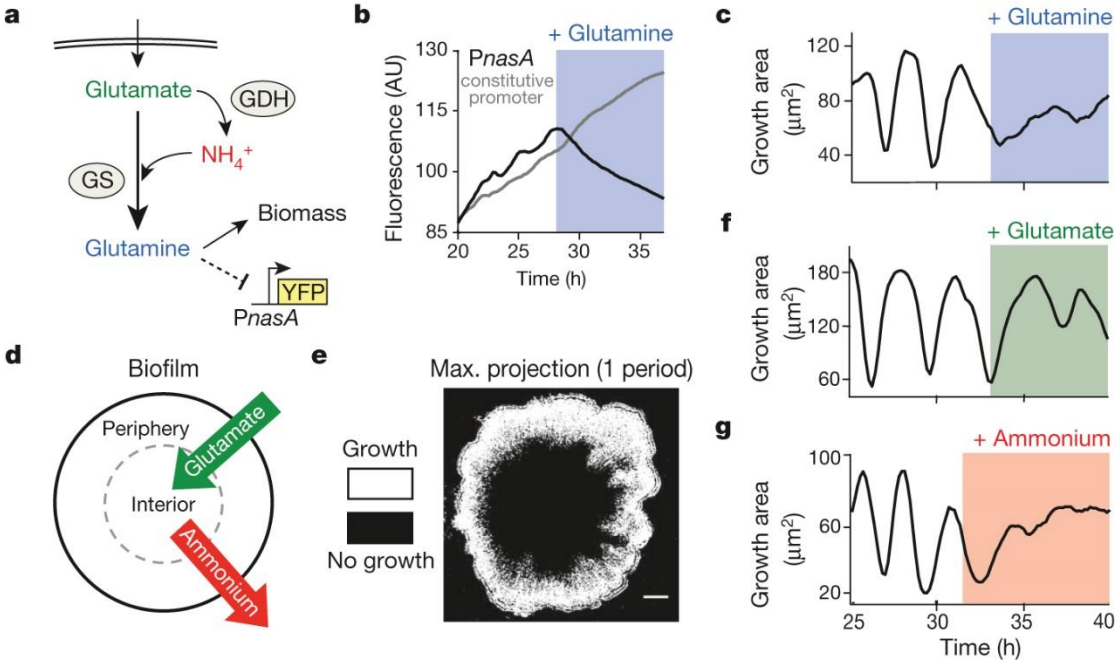

Figure 1.2. Biofilm growth depends specifically on extracellular ammonium availability. **a,** Colony growth in MSgg medium depends on the production of glutamine from externally supplied glutamate and self-produced or scavenged ammonium. Glutamine limitation was monitored using YFP expressed from the *nasA* promoter, which is activated upon glutamine limitation[21]. **b,** Addition of 1 mM glutamine (blue shading) represses expression from the P*nasA*-YFP reporter (black), but does not affect expression from a constitutive reporter (P*hyperspank*-CFP + 1 mM IPTG, gray). **c,** Growth area (see Methods: Data Analysis) before and after addition of 1 mM glutamine to an oscillating colony. **d,** Of the two nutrients required for glutamine production, externally supplied glutamate (green) is most abundant in the biofilm periphery, while biofilm-produced ammonium (red) is most abundant in the biofilm interior. **e,** Maximum intensity projection over one period of a colony oscillation, made from a difference movie (Methods: Data Analysis), which shows regions of growth (white) and no growth (black). Scale bar represents 100 μm. **f,** Growth area of an oscillating colony before and after addition of 30 mM glutamate (green shading). **g,** Growth area of an oscillating colony before and after addition of 1 mM ammonium (red shading).

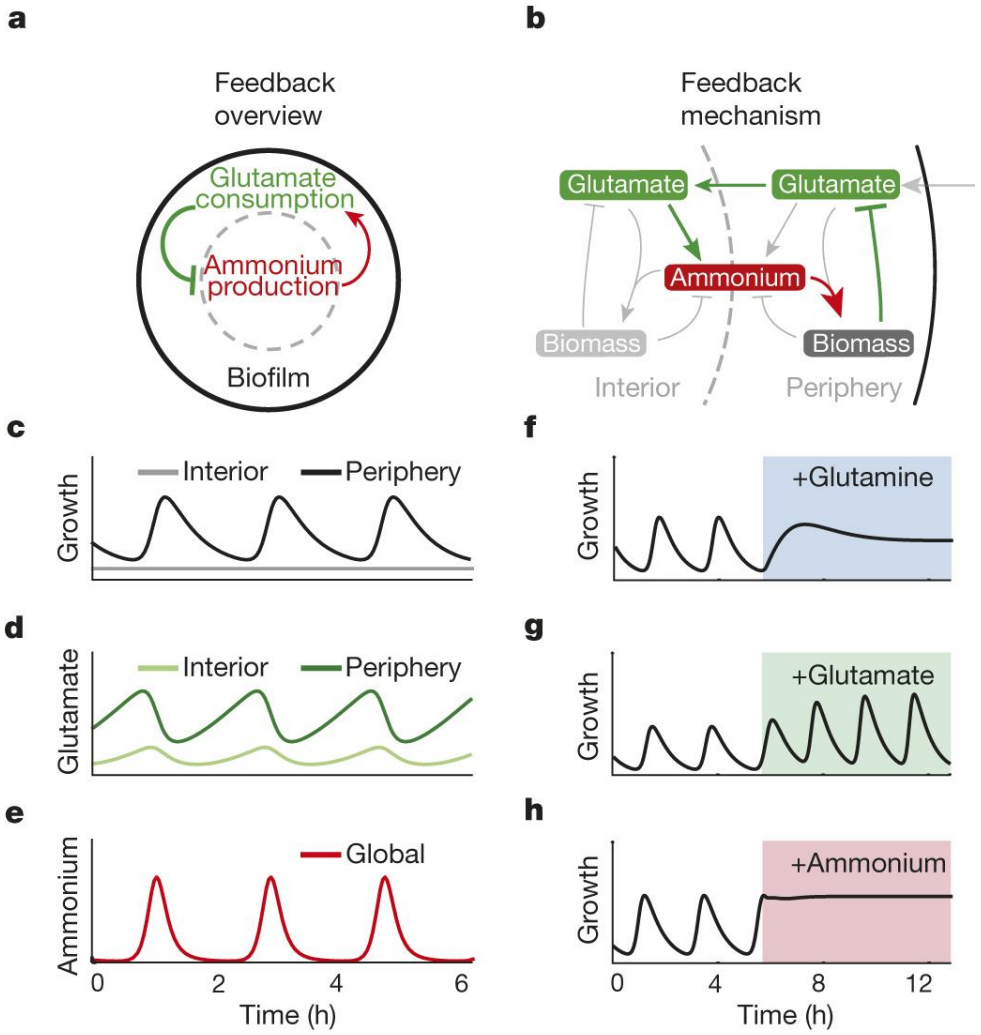

Figure 1.3. Mathematical modeling of a spatial metabolic feedback loop gives rise to oscillations consistent with experimental data. **a,** The production of ammonium in the interior is limited by and at the same time triggers the consumption of glutamate in the periphery (green and red arrows, respectively), producing a delayed negative feedback loop. **b,** The excess glutamate not consumed by the biofilm periphery diffuses to the interior, where it can be converted into ammonium (green arrows). The ammonium in turn enhances growth in the periphery (red arrow) and consequently reduces the supply of glutamate to the interior. Model predictions are shown in (**c**-**h**): **c,** Biofilm growth over time. **d,** Glutamate concentration over time. **e,** Ammonium concentration over time. **f,** Colony growth before and after glutamine addition (indicated by blue shading). **g,** Colony growth before and after addition of glutamate (green shading). *(h)* **h,** Colony growth before and after addition of ammonium (red shading).

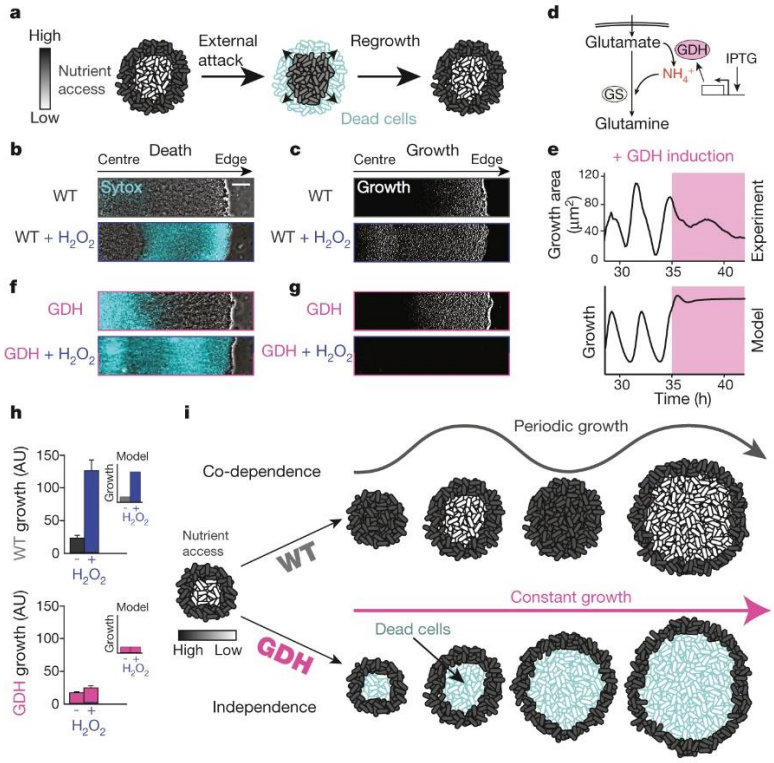

Figure 1.4. Metabolic codependence between interior and peripheral cells gives rise to oscillations that make the colony more resilient to external attack. **a,** Visual representation of the predicted outcome of an external attack on biofilm growth. **b,** Phase contrast merged with cell death marker (cyan, 1 µM Sytox Green) images of a wild type biofilm region shows cell death with and without challenge by 2% w/w H_2O_2. Scale bar represents 50 µm. **c,** In the same biofilm, difference images (white regions indicate cell growth) show wild type growth with and without challenge by H_2O_2. **d,** Overexpression of glutamate dehydrogenase (GDH, pink) promotes more production of ammonium from glutamate. **e,** Experimental (top) and modeling results (bottom) of GDH overexpression (induced with 1 mM IPTG, indicated by pink shading). **f,** Phase contrast merged with cell death marker (cyan, 1 µM Sytox Green) images of a colony overexpressing GDH with and without challenge by H_2O_2. **g,** In the same biofilm, difference images show cell growth during GDH overexpression alone, and with challenge by H_2O_2. **h,** Quantification of total biofilm growth rate in wild type (upper, *n* = 4 colonies) and GDH overexpression (lower, *n* = 3 colonies) strains upon challenge with H_2O_2. Error bars represent standard deviations. Modeling data are shown as an inset for each strain. **i,** Codependence between interior and peripheral cells exhibited in a wild type strain results in a growth strategy that sustains the viability of interior cells, while independence enforced by a GDH overexpression strain results in starvation of interior cells and reduced resilience to external attack.

Chapter 1.8 - Supplemental Figures

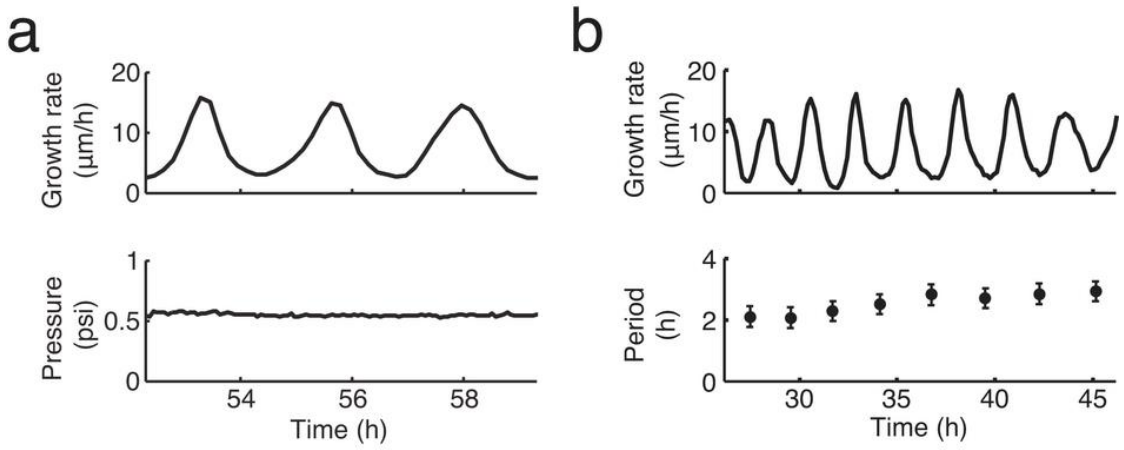

Figure S1.1. Characterization of biofilm growth oscillations. **a,** (Top) Growth rate over time of an oscillating colony. (Bottom) The pressure that drives media flow in the microfluidic chamber is constant over time (see Methods: Microfluidics). **b,** (Top) Growth rate of an oscillating colony. (Bottom) Period of each oscillation cycle, measured peak to peak. The error bars (±20 min) are determined by the imaging frequency (1 frame/10 min). The period slightly increases over time (see also Supplemental Fig. 6f and Methods: Mathematical Model).

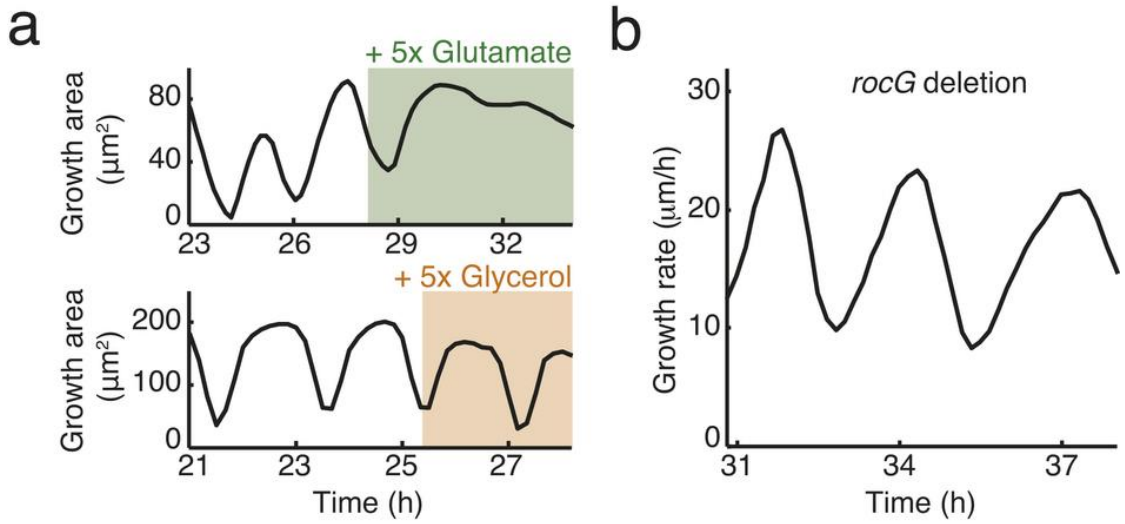

Figure S1.2. Roles of carbon and nitrogen in biofilm growth oscillations. **a,** Effect of increasing carbon (glycerol) or nitrogen (glutamate) availability on the oscillations. While increasing glutamate by 5 times of the normal MSgg levels leads to quenching of the oscillation, increasing glycerol by 5 times does not. **b,** Colony growth of mutant strain with *rocG* deletion. *B. subtilis* NCIB 3610 has two glutamate dehydrogenases (GDH), *rocG* and *gudB*. While *gudB* is constitutively expressed, *rocG* expression is subject to carbon catabolite repression[18]. The oscillatory growth of the *rocG* deletion strain indicates that carbon-source dependent regulation of *rocG* expression is not required for biofilm oscillations.

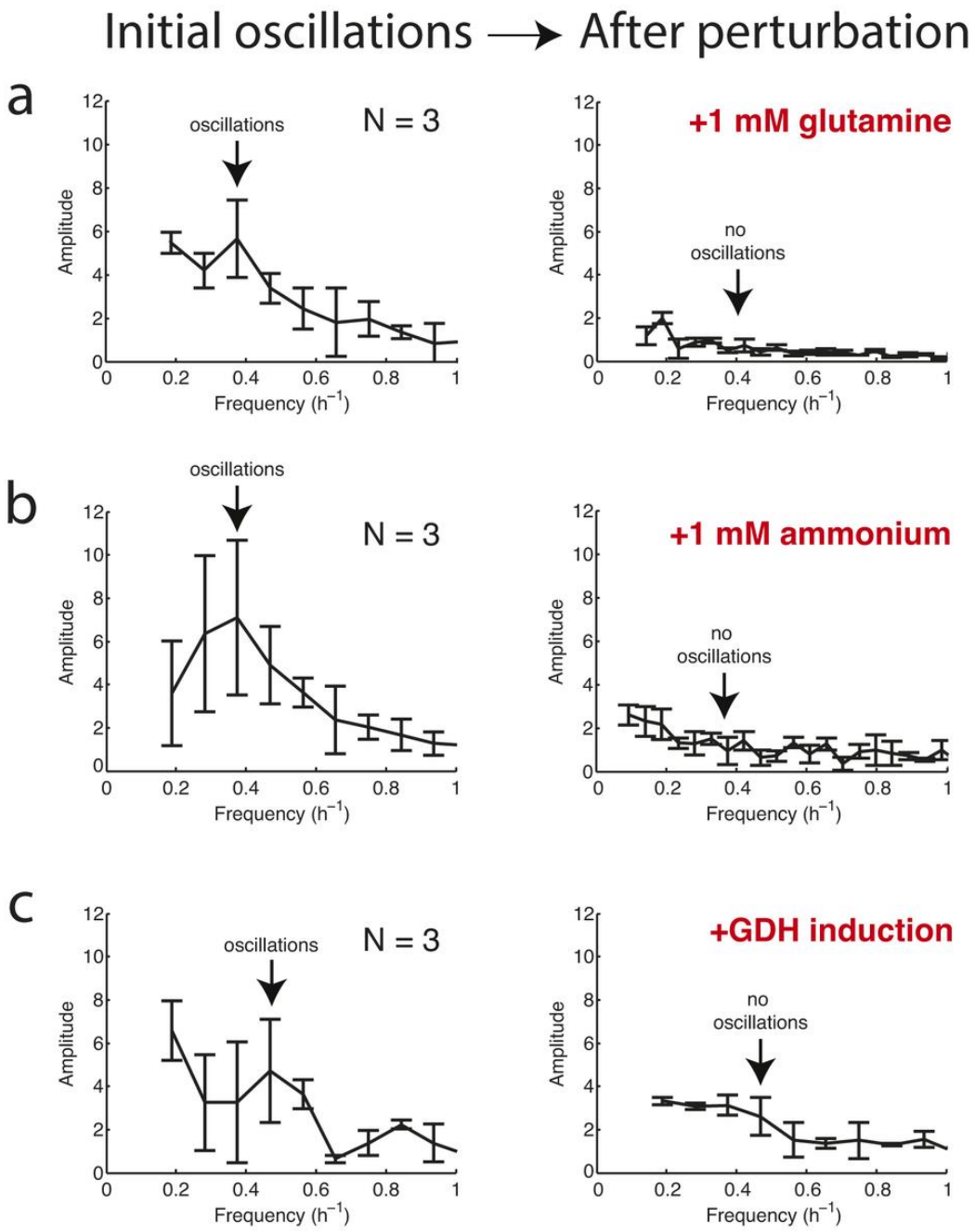

Figure S1.3. Fourier transform of biofilm growth rates before and after addition of **a,** 1 mM glutamine, **b,** 1 mM ammonium, and **c,** 1 mM IPTG to induce P*hyperspank*-RocG. The error bars show standard deviations (*n* = 3 colonies for each condition). The arrows indicate the frequency of oscillations for each condition before perturbation (left) and the lack of oscillations after perturbation (right).

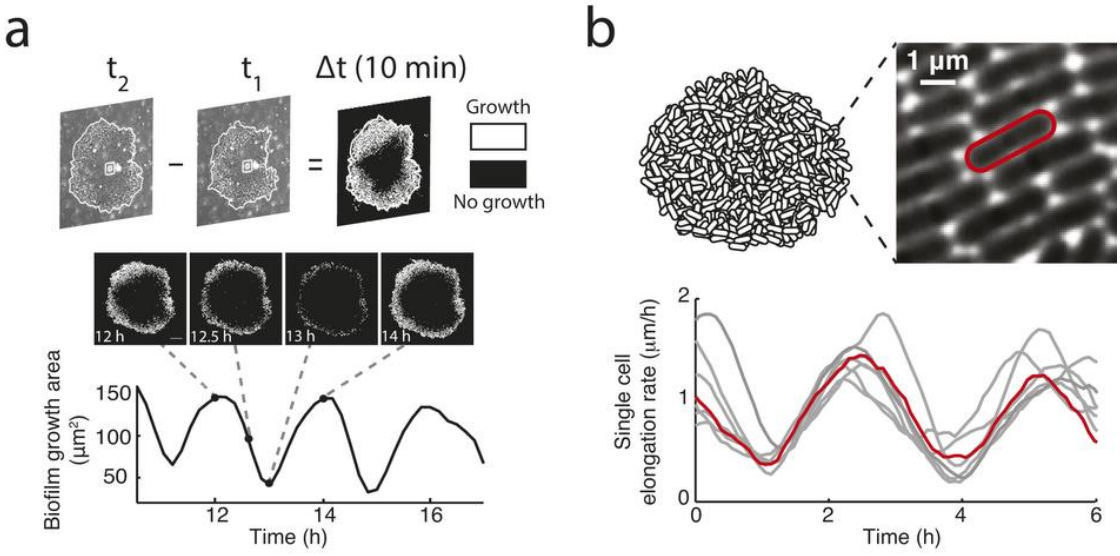

Figure S1.4. Measurements of cell growth within oscillating biofilms. **a,** (Top) Visual representation of the method through which difference movies are generated (Methods: Data Analysis). Growth is represented by white pixels, and lack of growth is indicated by black pixels. (Middle) Film strip and (bottom) growth area over time of an oscillating colony. Dashed lines show the position of each image on the time trace. Scale bar represents 100 μm. **b,** (Top left) schematic of a biofilm. (Top right) high magnification phase contrast image of biofilm periphery focused at the bottom layer of cells. (Bottom panel) time traces depicting elongation rates of single cells in gray. Highlighted in red is the single cell time trace for the cell outlined in red in the top right panel. The periodic slowdown of the growth of individual peripheral cells is responsible for the observed periodic reduction in biofilm expansion.

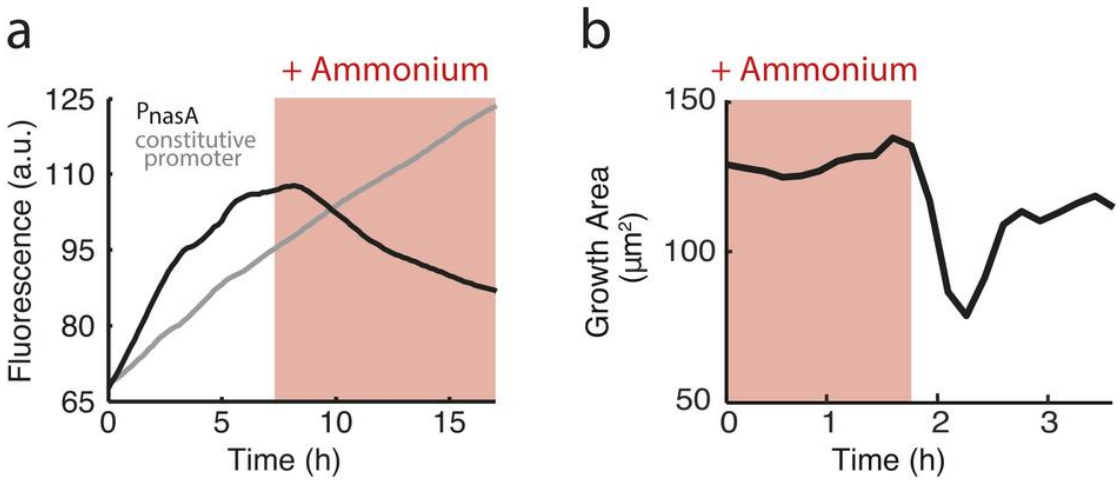

Figure S1.5. Effects of external ammonium on biofilm development. **a,** Addition of external ammonium (red shading, 1 mM) represses expression from the P*nasA*-YFP reporter (black), but does not affect expression from a constitutive reporter (P*hyperspank*-CFP + 1 mM IPTG, gray). **b,** Removal of external ammonium (red shading, 13 mM) causes halting of colony growth.

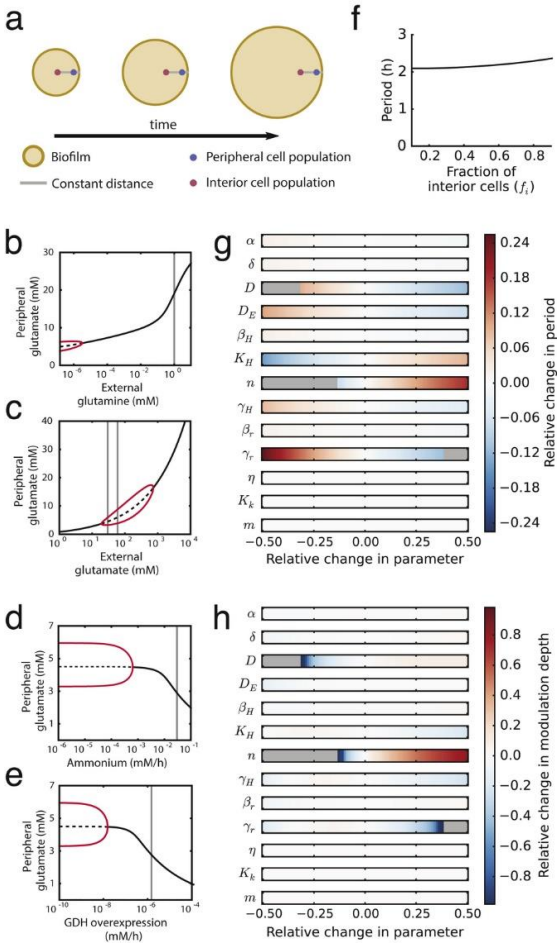

Figure S1.6. Mathematical model of biofilm growth. **a,** The model describes the dynamics of two cell populations in a biofilm, interior and peripheral. As the biofilm grows, there is a constant distance between the interior population and the biofilm edge. **b-e,** Bifurcation diagrams showing systematic analysis on the effects of external glutamine, external glutamate, ammonium uptake, and GDH overexpression respectively. The red lines correspond to the extrema of oscillations in peripheral glutamate (stable limit cycle). The solid black line denotes stable fixed point. The dashed black line corresponds to an unstable fixed point. The vertical gray lines highlight the state of the system for each nutrient addition experiment shown in Fig. 3 of the main text. **f,** Model prediction of oscillation period as function of interior cell fraction in the whole biofilm. **g-h,** Sensitivity analysis of oscillation period and modulation depth to changes in model parameters. Modulation depth is defined as the amplitude of the oscillations divided by the mean value. Gray color denotes parameter regions where the system does not oscillate.

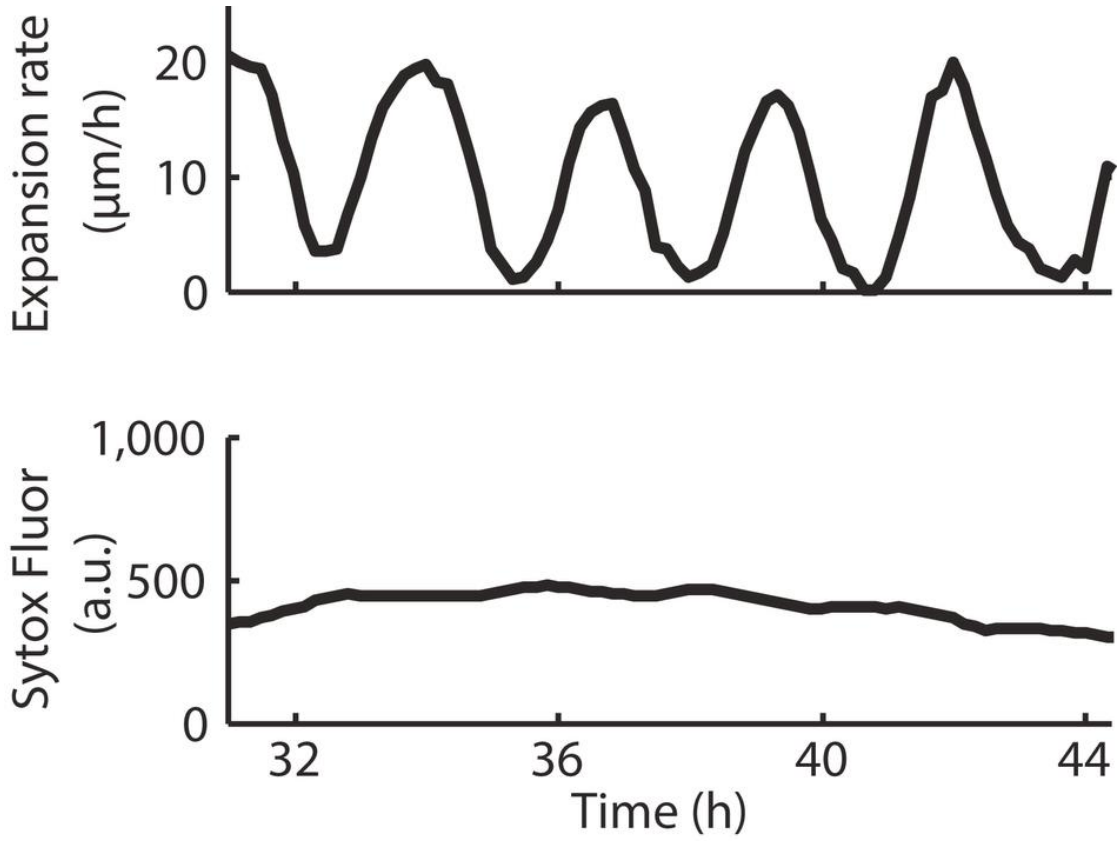

Figure S1.7. Temporal profile of cell death within an oscillating biofilm. **a,** Colony growth rate. **b,** Average fluorescence intensity of a cell death marker (Sytox Green, 1 μM, Life Technologies) from the same colony shown in (**a**).

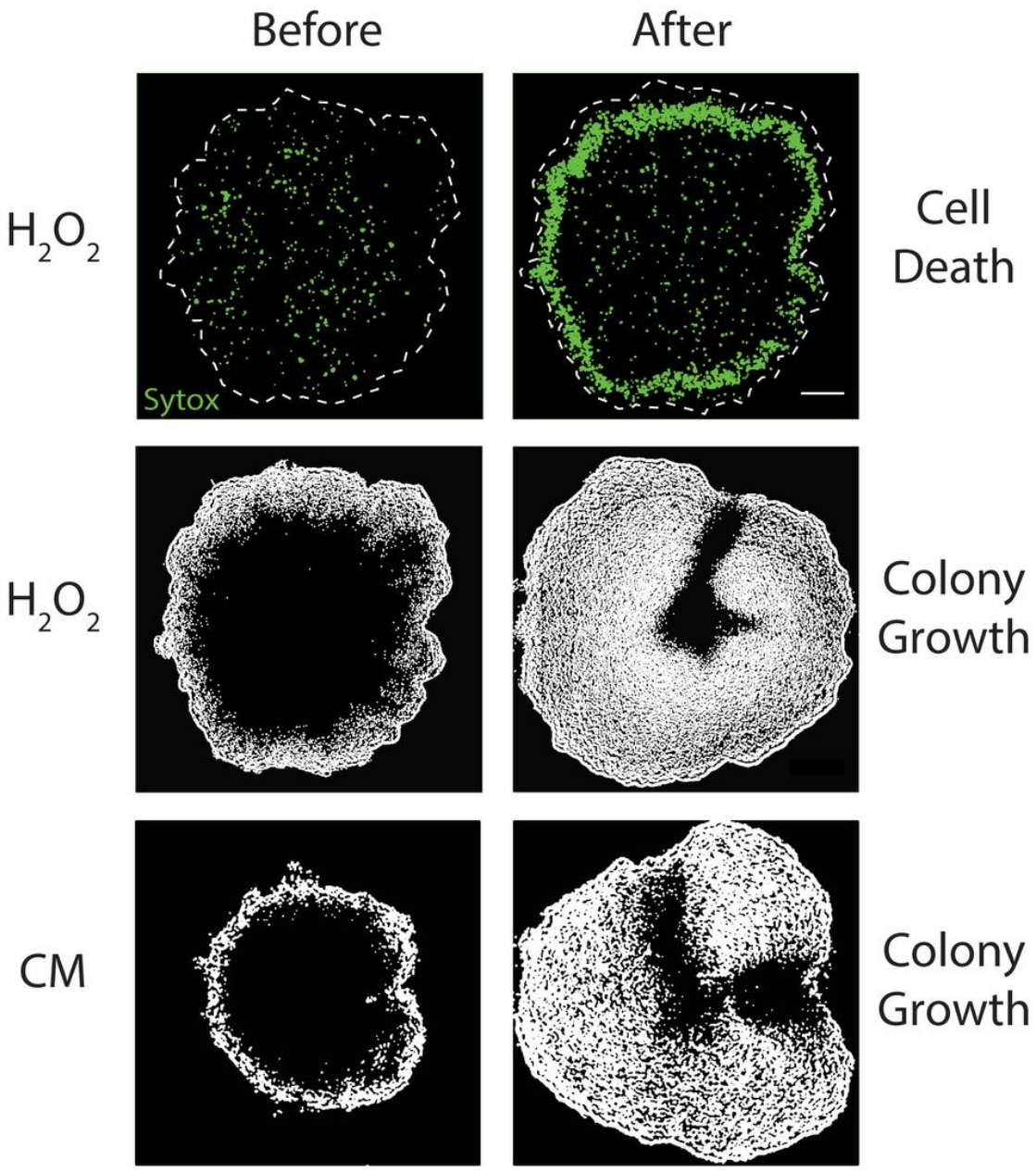

Figure S1.8. Effect of external attack with hydrogen peroxide (H_2O_2, 0.15% v/v) or chloramphenicol (CM, 5 µg/ml). (Top) cell death shown by Sytox Green (1 µM). (Middle and bottom) colony growth shown by image differencing (see Supplemental Fig. 4a and Methods: Data Analysis). Scale bar represents 100 µm. The white dashed lines indicate colony edge.

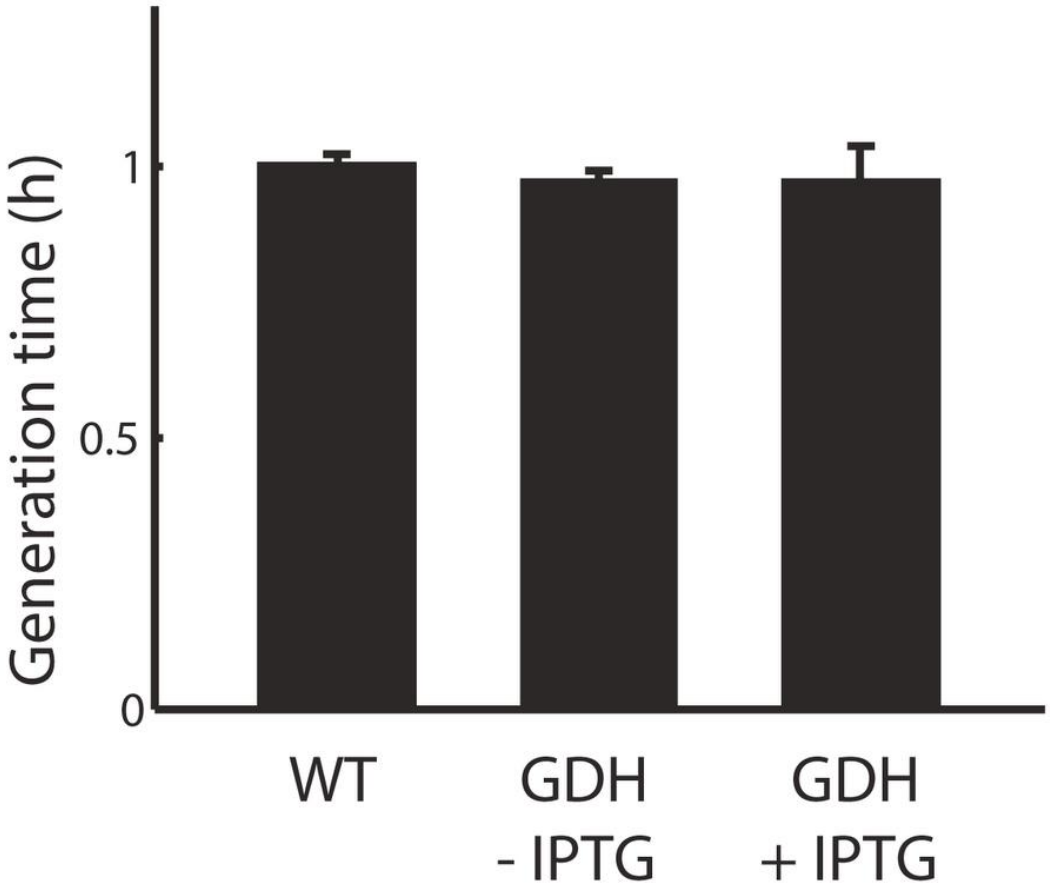

Figure S1.9. Effect of GDH induction on cell growth. Wild type and P*hyperspank*-RocG (uninduced or induced with 10 mM IPTG) strains were grown in liquid culture (MSgg medium, 30°C). Cell generation times were measured using OD_{600}. Error bars show standard deviations (*n* = 3 replicates).

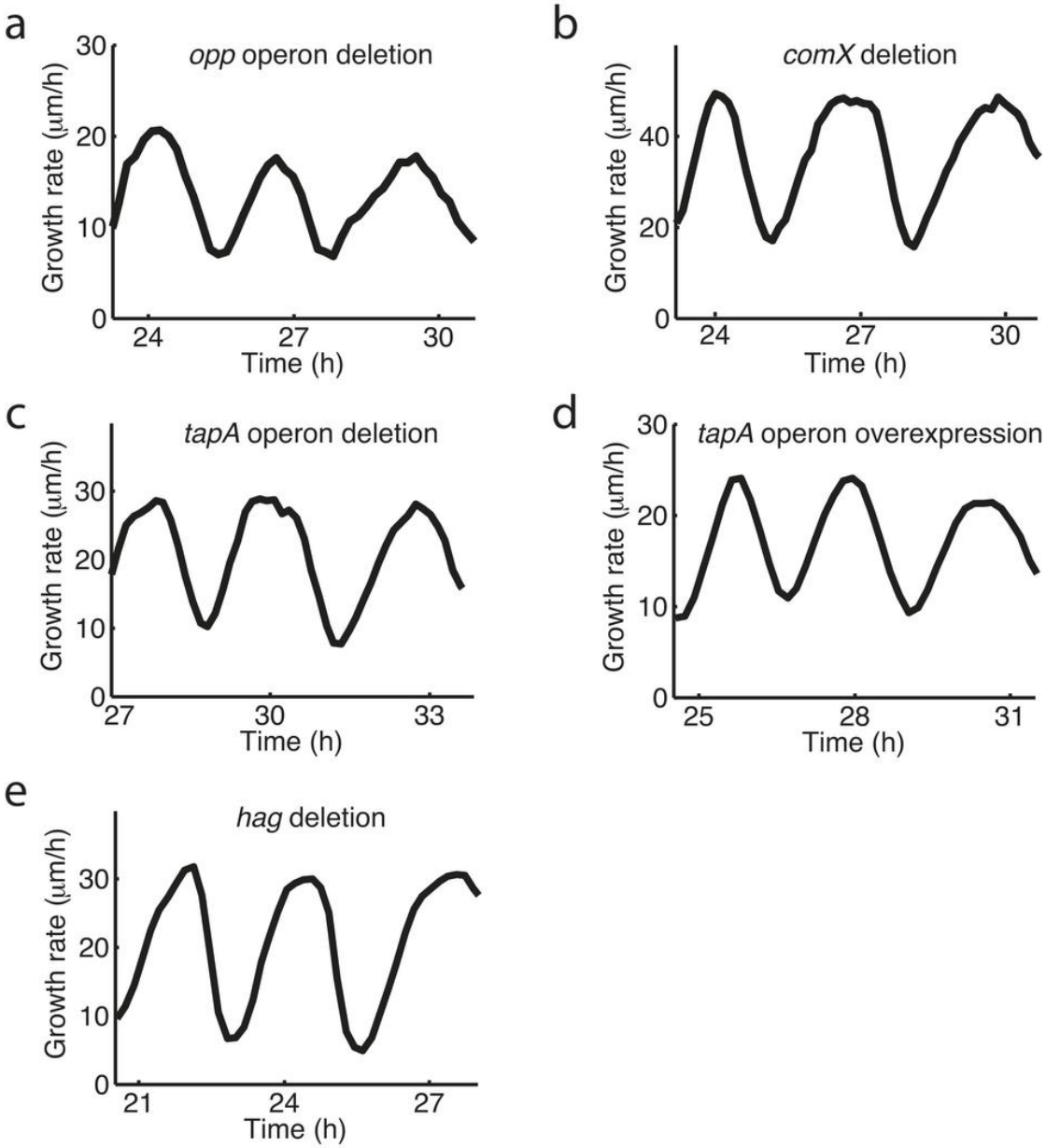

Figure S1.10. Growth rate oscillations persist in various mutant strains. **a,** *opp* operon deletion (deficient in quorum sensing). **b,** *comX* deletion (deficient in quorum sensing). **c,** *tapA* operon deletion (extracellular matrix component deletion). **d,** *tapA* operon overexpression (P*hyperspank*-tapA operon, 1mM IPTG). **e,** *hag* deletion (deficient in swimming and swarming). These results show that the corresponding genes and processes are not required for biofilm oscillations.

Chapter 1.9 – Methods

Strains:

All experiments were done using *Bacillus subtilis* NCIB 3610. The wild type strain was a gift from Wade Winkler (University of Maryland)[30], and all other strains were derived from it and are listed in Table S1. The pSac-CM-P*nasA*-*yfp* vector was a gift from Michael Elowitz (California Institute of Technology). To make over-expression strains, we used polymerase chain reaction (PCR) to amplify the desired region from the wild type strain. The PCR product is then put under the Hyper-spank promoter, using the HindIII/SalI and the NheI sites within the pDR111 vector (gift from David Rudner, Harvard Medical School). The Hyper-spank promoter controls over-expression of the gene through isopropyl-β-D-thiogalactopyranoside (IPTG) induction. Vectors for deletion strains were made in a similar way using the pER449 plasmid (gift from Wade Winkler). All constructs were confirmed by direct sequencing and then integrated into the chromosome of the wild type strain by a standard one-step transformation procedure. Finally, chromosomal integrations were confirmed by colony PCR using the corresponding primers.

Table S1.1. List of strains used in chapter 1

Strain	Genotype	Source
Wild type	*B. subtilis* NCIB 3610	*30*
P_{hyp}-*CFP*, P_{nasA}-*YFP*	*amyE::* $P_{Hyper\text{-}spank}$-*CFP*, *sacA::* P*nasA*-*YFP* (Sp^R, Cm^R)	This study
P_{hyp}-*rocG*	*amyE::* $P_{Hyper\text{-}spank}$-*rocG* (Sp^R)	This study
P_{hyp}-*tapA operon*	*amyE::* $P_{Hyper\text{-}spank}$-*tapA operon* (Sp^R)	This study
ΔtapA operon	*tapA-sipW-tasA::* cat	This study
ΔoppA-D	*oppABCD::* cat	This study
ΔcomX	*comX::* cat	*17*
Δhag	*hag::* cat	This study
ΔrocG	*rocG::* kan	This study

Growth conditions:

The biofilms were grown using MSgg medium[16]. It contains 5 mM potassium phosphate buffer (pH 7.0), 100 mM MOPS buffer (pH 7.0, adjusted using NaOH), 2 mM $MgCl_2$, 700 µM $CaCl_2$, 50 µM $MnCl_2$, 100 µM $FeCl_3$, 1 µM $ZnCl_2$, 2 µM thiamine HCl, 0.5% (v/v) glycerol and 0.5% (w/v) monosodium glutamate. The MSgg medium was made from stock solutions on the day of the experiment, and the stock solution for glutamate was made new each week.

Microfluidics:

We used the CellASIC ONIX Microfluidic Platform and the Y04D microfluidic plate (EMD Millipore). It provides unconventionally large chambers, allowing the formation of colonies containing millions of cells, yet still leaves room for media flow. Media flow in the microfluidic chamber was driven by a pneumatic pump from the CellASIC ONIX Microfluidic Platform, and the pressure from the pump was kept stable during the course of the oscillation. In most of the experiments, we used a pump pressure of 1 psi with only one media inlet open (there are 6 media inlets in the Y04D plate), which corresponds to a flow speed of ~16 μm/s in the growth chamber.

On the day before the experiment, cells from −80°C glycerol stock were streaked onto LB agar plate and incubated at 37°C for overnight. The next day morning, a single colony was picked from the plate and inoculated into 3 ml of LB broth in a 50 ml conical tube, and then incubated in 37°C shaker. After 2.5 hours of incubation, the cell culture was centrifuged at 2100 rcf for 1 min, and then the cell pellet was re-suspended in MSgg and then immediately loaded into microfluidics. After the loading, cells in the microfluidic chamber were incubated at 37°C for 90 min, and then the temperature was kept at 30°C for the rest of the experiment.

Time-Lapse Microscopy:

The growth of the biofilms was recorded using phase contrast microscopy. The microscopes used were Olympus IX81 and IX83, and DeltaVision PersonalDV. To image entire biofilms, 10X lens objectives were used in most of the experiments. Images were

taken every 10 min. Whenever fluorescence images were recorded, we used the minimum exposure time that still provided a good signal-to-noise ratio.

Biofilm growth rate:

ImageJ (National Institutes of Health) and MATLAB (MathWorks) were used for image analysis. In house software was also developed to perform colony detection and quantification of colony expansion. Multiple methods of colony detection were used to ensure the accuracy of the analysis. To detect regions of expansion in a biofilm, we performed image differencing on snapshots of the biofilm from time-lapse microscopy videos. Specifically, we calculated the difference between two consecutive phase contrast images (taken 10 min apart) by finding the absolute difference between each pixel in each image. We then generated an image stack based on these results. The intensity values from the stack correlate with the expansion inside the biofilm. The growth area was determined by converting difference images to binary images and then measuring the area of the colony growth region (white pixels). To measure cell replication time, we tracked the length and division of individual cells in the biofilm periphery (**Fig. S1.4b**).

Mathematical model of metabolic codependence:

Model description:

We describe the dynamics of biofilm growth in terms of two distinct populations, corresponding to the interior and the periphery of the biofilm. The two populations are assumed to be located in a moving frame of reference as the biofilm grows, so that they are always located at the same distance from the physical edge of the biofilm (Extended Data Figure 6a).

The metabolic state of the biofilm is described by the following quantities: 1) The concentrations of glutamate G_i in the interior and G_p in the periphery of the biofilm; 2) The concentration A of ammonium in the biofilm, which is assumed to be equal for the two populations due to its fast diffusion; 3) The concentration H_i of active glutamate dehydrogenase (GDH) in the interior cells; and 4) the rate of biomass production, which is assumed to be given by the concentrations of housekeeping proteins (such as ribosomal proteins) in the interior (r_i) and in the periphery (r_p). The dynamics of these state variables are described by the following set of ordinary differential equations:

$$\frac{dA}{dt} = \alpha G_i H_i - \delta_A A(r_i + r_p)$$

$$\frac{dG_i}{dt} = D\left(G_p - G_i\right) - \alpha G_i H_i - \delta_G G_i r_i$$

$$\frac{dG_p}{dt} = D\left(G_i - G_p\right) + D_E\left(G_E - G_p\right) - \delta_G G_p r_p$$

$$\frac{dH_i}{dt} = \beta_H \frac{G_i^n}{K_H^n + G_i^n} - \gamma_H H_i$$

$$\frac{dr_i}{dt} = \beta_r A G_i - \gamma_r r_i$$

$$\frac{dr_p}{dt} = \beta_r A G_p - \gamma_r r_p$$

The terms in the equations are interpreted as follows:

- $\alpha G_i H_i$: ammonium production from glutamate, catalyzed by the enzyme GDH (Figure 2a)
- $\delta_A A(r_i + r_p)$: ammonium consumption by interior and peripheral cells
- $\delta_G G_i r_i$ and $\delta_G G_p r_p$: glutamate consumption by interior and peripheral cells, respectively
- $D(G_p - G_i)$: glutamate diffusion between peripheral and interior regions
- $D_E(G_E - G_p)$: glutamate diffusion between the environment and the periphery of the biofilm
- $\beta_H \frac{G_i^n}{K_H^n + G_i^n}$: GDH activation in the interior cells
- $\gamma_H H_i$: GDH deactivation in the interior cells
- $\beta_r A G_i$ and $\beta_r A G_p$: production of housekeeping proteins in the interior and peripheral cells, respectively
- $\gamma_r r_i$ and $\gamma_r r_p$: degradation of housekeeping proteins in interior and peripheral cells, respectively

We make the following assumptions:

- Peripheral cells rely on ammonium synthesized by interior cells. As a simplification, we assume only the interior cells have active GDH.
- Activation of GDH is strongly reduced when the concentration of available glutamate is below a given threshold. This can be due to explicit regulatory interactions or simply as a consequence of the slowdown of cellular processes in the absence of nutrients.
- Consumption of ammonium and glutamate depends on the metabolic activity of the cell. The higher the concentration of housekeeping proteins – a proxy for the metabolic state of the cell – the faster the consumption of nutrients.
- The production of housekeeping proteins increases with the concentrations of glutamate and ammonium.

In order to extract from the model the population expansion, which can be measured experimentally, we consider that the dynamics of the cell density $\boldsymbol{\rho}$ of the two populations are given by:

$$\frac{d\rho_{i,p}}{dt} = \eta r_{i,p}\rho_{i,p}\left(1 - \frac{\rho_{i,p}}{K(G_{i,p})}\right) - \lambda_{i,p}\rho_{i,p}$$

The first term in the right-hand side is a logistic-growth term, where the maximal growth rate is considered to be proportional to the concentrations of housekeeping proteins r_i and r_p. Additionally, we assume that the carrying capacity K depends on the concentration of glutamate:

$$K(G) = \frac{G^m}{K_k^m + G^m}$$

Thus $K(G)$ varies between 0 and 1 depending on whether glutamate concentration is below or above a given threshold, denoted as K_k. Note that the cell density $\rho_{i,p}$ defined here is relative to the carrying capacity, therefore, both K and ρ are dimensionless.

The logistic-growth term in the density equation shown above describes the standard birth/death processes that occur in an unmoving bacterial population. In our system, however, the peripheral cells are always expanding into the open area outside of the biofilm. We represent this fact by adding an effective decay term, $-\lambda_{i,p}\rho_{i,p}$, to the right-hand side of the density equation of the expanding population (i.e. the peripheral population for all situations considered, except in the case of chemical attack, where the peripheral population is eradicated and consequently the interior cells can expand). This decay term accounts for the effective loss of cells undergone locally by the biofilm front as it expands (in our moving reference frame) into the cell-free area surrounding it.

Given the above-described dynamics for the cell densities, the growth rate (measured experimentally as the area of non-zero local motion within the biofilm) is given by the logistic term, since this is the only term related with actual growth of the population:

$$\mu_{i,p} = \eta r_{i,p} \rho_{i,p} \left(1 - \frac{\rho_{i,p}}{K(G_{i,p})}\right)$$

Addition of glutamine to the media:

Glutamine is synthesized by glutamine synthase (GS) in the cell, and it also regulates the activity of GS through negative feedback [27]. Therefore, external addition of glutamine reduces GS activity, and consequently lowers its consumption of ammonium and glutamate (used to synthesize glutamine). Additionally, we assumed that glutamine inhibits either directly or indirectly GDH activity, affecting the production of ammonium from glutamate. This is implemented in the model as non-competitive inhibition on the parameters α and δ. Specifically, the effective $\bar{\alpha}$ and $\bar{\delta}$ are given by:

$$\bar{\alpha} = \frac{\alpha}{\frac{[Gln]}{K_\alpha} + 1}, \qquad \overline{\delta_{A,G}} = \frac{\delta_{A,G}}{\frac{[Gln]}{K_\delta} + 1}$$

Figure 3f in the main text shows the model prediction: in agreement with the experimental observations, external addition of glutamine leads to the quenching of oscillation. A systematic analysis of the effect of glutamine addition is shown in

Extended Data Fig. 5b, where a bifurcation diagram of the peripheral glutamate concentration with respect to the added glutamine concentration is shown.

Addition of glutamate to the media:

The concentration of glutamate in the external medium is explicitly defined in the model by the parameter G_E. Thus, supplementation of additional glutamate is straightforward in the model – it increases the value of G_E. Figure 3g in the main text shows the model prediction: consistent with the experimental observations, a moderate increase in external glutamate does not eliminate the oscillations. A systematic study also shows that further increasing glutamate leads to quenching of oscillations (Extended Data Fig. 5c).

Addition of ammonium to the media:

The concentration of ammonium is explicitly represented in the model with the variable A, and addition of ammonium to the media can be represented as an additional creation term (α_0) in the ammonium equation:

$$\frac{dA}{dt} = \alpha G_i H_i - \delta_A A(r_i + r_p) + \boldsymbol{\alpha_0}$$

Figure 3h in the main text shows the model prediction: in agreement with the experiments, externally adding ammonium quenches oscillation. We also

systematically explored the effect of different ammonium concentrations through a bifurcation diagram of the system with respect to α_0 (Extended Data Fig. 5d).

Overexpression of GDH in cells:

We also investigated the effects of overexpressing GDH in the biofilm. The overexpression is implemented in the model by an additional creation term β_0 in the equation for GDH (H_i). Furthermore, since the overexpression is applied throughout the entire biofilm, we now also need to include active GDH in the peripheral cells (H_p), and consequently the production of ammonium from those cells. To that end, the differential equations for A, G_p and H_i are modified as shown below, and an equation for GDH in the peripheral cell population (H_p) is also added:

$$\frac{dA}{dt} = \alpha G_i H_i + \boldsymbol{\alpha G_p H_p} - \delta_A A\left(r_i + r_p\right)$$

$$\frac{dG_p}{dt} = D\left(G_i - G_p\right) + D_E\left(G_E - G_p\right) - \boldsymbol{\alpha G_p H_p} - \delta_G G_p r_p$$

$$\frac{dH_i}{dt} = \boldsymbol{\beta_0} + \beta_H \frac{G_i^n}{K_H^n + G_i^n} - \gamma_H H_i$$

$$\boldsymbol{\frac{dH_p}{dt} = \beta_0 - \gamma_H H_p}$$

Figure 4e in the main text shows the model prediction: in agreement with the experiments, overexpressing GDH leads to quenching of oscillation. A systematic

analysis on different levels of overexpression is shown in the bifurcation diagram in the Extended Data Fig. 5e.

Addition of hydrogen peroxide to the media:

Hydrogen peroxide is a strong oxidizer that can kill the cells on the periphery of the biofilm. Dead cells in the biofilm will still affect glutamate diffusion but will be metabolically inactive. Thus, the killing is implemented in the model by removing the production term of housekeeping proteins in the peripheral cell population. Additionally, a new negative term in the cellular density equation is introduced to account for cell death. To that end, the differential equations for r_p and ρ_p are modified as shown below:

$$\frac{dr_p}{dt} = -\gamma_r r_p$$

$$\frac{d\rho_p}{dt} = \eta r_p \rho_p \left(1 - \frac{\rho_p}{K(G_p)}\right) - \boldsymbol{\lambda_{H_2O_2}\rho_p} - \lambda_p \rho_p$$

The new term is also added to the equation for the rate population expansion:

$$\mu_p = \eta r_p \rho_p \left(1 - \frac{\rho_p}{K(G_p)}\right) - \boldsymbol{\lambda_{H_2O_2}\rho_p}$$

Finally, in the case of GDH overexpression, hydrogen peroxide entirely eliminates GDH production in the peripheral cell population, and the differential equation for H_p becomes:

$$\frac{dH_p}{dt} = -\gamma_H H_p$$

Figure 4h in the main text shows the model prediction on the average growth rate and death in interior and peripheral populations after the addition of hydrogen peroxide, for both wild type and GDH overexpressing biofilms.

Effect of varying the ratio of interior to peripheral cells:

As a consequence of biofilm expansion the relative size of interior and peripheral cell populations changes over time. Since the variables of the mathematical model represent intensive quantities (their value does not depend on the total volume) most of the equations would not be affected by changes in the relative size of both cell populations. The only exception is the equation for ammonium, as it describes the concentration of this species in the whole biofilm, taking into account reactions that occur exclusively in one or the other population region. In this case the relative size of each one of these two regions will modulate the relative effect of these reactions.

To explore the effects of changes in the relative sizes of the two populations, we define f_i as the fraction of the size of the interior population over the whole biofilm population. This parameter allows us to distinguish the contributions of the interior and peripheral regions to both the production and the consumption of ammonium:

$$\frac{dA}{dt} = f_i \alpha G_i H_i - \delta_A A\left(f_i r_i + (1 - f_i)\, r_p\right)$$

This equation allows us to determine the effect of an increase in f_i (such as the one that occurs in the biofilm as it expands) on the growth oscillations reported above.

Extended Data Figure 6f shows that the oscillations persist for a wide range of f_i values, with a period that increases only slightly with f_i, in agreement with the experimental observations.

Sensitivity analysis:

Extended Data Figure 6g and h show how changes in each one of the intrinsic parameters of the model affect the period and the modulation depth of the oscillations. The values of the parameters were scanned from 50% to 150% of its original value. Whenever a modulation depth lower than 2% was measured the system was considered to be non-oscillating, and labeled in gray in the color plot.

Table S1.2: The parameter values used in the paper.

	Description	**Value**	**Units**
α	Glutamate dehydrogenation coefficient	50	$\mu M^{-1}\ h^{-1}$
δ_A	Ammonium consumption coefficient	4	$\mu M^{-1}\ h^{-1}$
δ_G	Glutamate consumption rate	4	$\mu M^{-1}\ h^{-1}$
D	Glutamate diffusion constant within the biofilm.	0.4	h^{-1}
D_E	Glutamate diffusion constant between biofilm and exterior	0.6	h^{-1}
G_E	Glutamate concentration in the external medium	30	mM
β_H	Maximal activation rate of GDH	50	$\mu M\ h^{-1}$
γ_H	Deactivation rate of GDH	7.5	h^{-1}
K_H	GDH activation threshold	7.2	mM
n	Hill coefficient for GDH activation	7	
β_r	Expression coefficient of ribosomal/housekeeping proteins.	0.14	$mM^{-1}\ h^{-1}$
γ_r	Degradation rate of ribosomal/housekeeping proteins	2	h^{-1}
η	Population growth rate coefficient	100	mM^{-1}
K_K	Glutamate threshold for carrying capacity	0.85	mM
m	Hill coefficient for carrying capacity	12	
λ_i	Expansion rate of interior cells	0	h^{-1}
λ_p	Expansion rate of peripheral cells	0.032	h^{-1}
$[Gln]$	Concentration of glutamine in the medium	1	mM
K_α	Glutamine inhibition threshold on GDH activity	$5{\cdot}10^{-8}$	mM
K_δ	Glutamine inhibition threshold on GS activity	$5{\cdot}10^{-2}$	mM
α_0	Rate of ammonium entering the biofilm from the external medium	0.03	$mM\ h^{-1}$
β_0	Expression rate of GDH from the additional copy of the gene	$1.5{\cdot}10^{-6}$	$mM\ h^{-1}$
$\lambda_{H_2O_2}$	Death rate due to hydrogen peroxide	5	h^{-1}

Chapter 1.10 – Works cited in chapter 1

Anyan, M. E., Amiri, A., Harvey, C. W., Tierra, G., Morales-Soto, N., Driscoll, C. M., Alber, M. S., and Shrout, J. D. (2014) Type IV pili interactions promote intercellular association and moderate swarming of Pseudomonas aeruginosa, *Proceedings of the National Academy of Sciences of the United States of America 111*, 18013-18018.

Asally, M., Kittisopikul, M., Rue, P., Du, Y., Hu, Z., Cagatay, T., Robinson, A. B., Lu, H., Garcia-Ojalvo, J., and Suel, G. M. (2012) Localized cell death focuses mechanical forces during 3D patterning in a biofilm, *Proceedings of the National Academy of Sciences of the United States of America 109*, 18891-18896.

Belitsky, B. R., and Sonenshein, A. L. (1998) Role and regulation of Bacillus subtilis glutamate dehydrogenase genes, *Journal of bacteriology 180*, 6298-6305.

Ben-Jacob, E., Cohen, I., and Levine, H. (2000) Cooperative self-organization of microorganisms, *Adv Phys 49*, 395-554.

Berk, V., Fong, J. C., Dempsey, G. T., Develioglu, O. N., Zhuang, X., Liphardt, J., Yildiz, F. H., and Chu, S. (2012) Molecular architecture and assembly principles of Vibrio cholerae biofilms, *Science 337*, 236-239.

Boogerd, F. C., Ma, H. W., Bruggeman, F. J., van Heeswijk, W. C., Garcia-Contreras, R., Molenaar, D., Krab, K., and Westerhoff, H. V. (2011) AmtB-mediated NH3 transport in prokaryotes must be active and as a consequence regulation of transport by GlnK is mandatory to limit futile cycling of NH4+/NH3, *Febs Lett 585*, 23-28.

Branda, S. S., Gonzalez-Pastor, J. E., Ben-Yehuda, S., Losick, R., and Kolter, R. (2001) Fruiting body formation by Bacillus subtilis, *Proceedings of the National Academy of Sciences of the United States of America 98*, 11621-11626.

Castorph, H., and Kleiner, D. (1984) Some properties of a Klebsiella pneumoniae ammonium transport negative mutant (Amt-), *Archives of microbiology 139*, 245-247.

Commichau, F. M., Gunka, K., Landmann, J. J., and Stulke, J. (2008) Glutamate metabolism in Bacillus subtilis: gene expression and enzyme activities evolved to avoid futile cycles and to allow rapid responses to perturbations of the system, *Journal of bacteriology 190*, 3557-3564.

Costerton, J. W., Stewart, P. S., and Greenberg, E. P. (1999) Bacterial biofilms: a common cause of persistent infections, *Science 284*, 1318-1322.

Davies, D. (2003) Understanding biofilm resistance to antibacterial agents, *Nature reviews. Drug discovery 2*, 114-122.

Detsch, C., and Stulke, J. (2003) Ammonium utilization in Bacillus subtilis: transport and regulatory functions of NrgA and NrgB, *Microbiology 149*, 3289-3297.

Donlan, R. M., and Costerton, J. W. (2002) Biofilms: survival mechanisms of clinically relevant microorganisms, *Clinical microbiology reviews 15*, 167-193.

Eldar, A. (2011) Social conflict drives the evolutionary divergence of quorum sensing, *Proceedings of the National Academy of Sciences of the United States of America 108*, 13635-13640.

Gregor, T., Fujimoto, K., Masaki, N., and Sawai, S. (2010) The Onset of Collective Behavior in Social Amoebae, *Science 328*, 1021-1025.

Gunka, K., and Commichau, F. M. (2012) Control of glutamate homeostasis in Bacillus subtilis: a complex interplay between ammonium assimilation, glutamate biosynthesis and degradation, *Molecular microbiology 85*, 213-224.

Hall-Stoodley, L., Costerton, J. W., and Stoodley, P. (2004) Bacterial biofilms: from the natural environment to infectious diseases, *Nature reviews. Microbiology 2*, 95-108.

Hibbing, M. E., Fuqua, C., Parsek, M. R., and Peterson, S. B. (2010) Bacterial competition: surviving and thriving in the microbial jungle, *Nature reviews. Microbiology 8*, 15-25.

Irnov, I., and Winkler, W. C. (2010) A regulatory RNA required for antitermination of biofilm and capsular polysaccharide operons in Bacillales, *Molecular microbiology 76*, 559-575.

Jayakumar, A., Schulman, I., MacNeil, D., and Barnes, E. M., Jr. (1986) Role of the Escherichia coli glnALG operon in regulation of ammonium transport, *Journal of bacteriology 166*, 281-284.

Kim, M., Zhang, Z., Okano, H., Yan, D., Groisman, A., and Hwa, T. (2012) Need-based activation of ammonium uptake in Escherichia coli, *Molecular systems biology 8*, 616.

Kleiner, D. (1985) Bacterial Ammonium Transport, *Fems Microbiol Lett 32*, 87-100.

Nakano, M. M., Yang, F., Hardin, P., and Zuber, P. (1995) Nitrogen regulation of nasA and the nasB operon, which encode genes required for nitrate assimilation in Bacillus subtilis, *Journal of bacteriology 177*, 573-579.

Oliveira, N. M., Niehus, R., and Foster, K. R. (2014) Evolutionary limits to cooperation in microbial communities, *Proceedings of the National Academy of Sciences of the United States of America 111*, 17941-17946.

Stannek, L., Thiele, M. J., Ischebeck, T., Gunka, K., Hammer, E., Volker, U., and Commichau, F. M. (2015) Evidence for synergistic control of glutamate biosynthesis by glutamate dehydrogenases and glutamate in Bacillus subtilis, *Environmental microbiology*.

Vlamakis, H., Aguilar, C., Losick, R., and Kolter, R. (2008) Control of cell fate by the formation of an architecturally complex bacterial community, *Genes & development 22*, 945-953.

Wilking, J. N., Zaburdaev, V., De Volder, M., Losick, R., Brenner, M. P., and Weitz, D. A. (2013) Liquid transport facilitated by channels in Bacillus subtilis biofilms, *Proceedings of the National Academy of Sciences of the United States of America 110*, 848-852.

Wingreen, N. S., and Levin, S. A. (2006) Cooperation among microorganisms, *Plos Biol 4*, 1486-1488.

Yildiz, F. H., and Visick, K. L. (2009) Vibrio biofilms: so much the same yet so different, *Trends in microbiology 17*, 109-118.

Zeigler, D. R., Pragai, Z., Rodriguez, S., Chevreux, B., Muffler, A., Albert, T., Bai, R., Wyss, M., and Perkins, J. B. (2008) The origins of 168, W23, and other Bacillus subtilis legacy strains, *Journal of bacteriology 190*, 6983-6995.

Chapter 1.11 – Acknowledgements

Chapter 1, in full, is a reprint of the material as it appears in Liu, J., Prindle, A., Humphries, J., Gabalda-Sagarra, M., Asally, M., Lee, D-Y., Ly, S., Garcia-Ojalvo, J., and Suel, G. M., Nature, 2015. The dissertation author was a co-author of this paper.

We would like to thank K. Süel, T. Çağatay, R. Wollman, T. Hwa and M. Elowitz for comments during the writing of the manuscript. A.P. is a Simons Foundation Fellow of the Helen Hay Whitney Foundation. J.H. is supported by the UCSD Cell and Molecular Genetics Training Grant. J.G.-O. is supported by the Ministerio de Economia y Competitividad (Spain) and FEDER, under project FIS2012-37655-C02-01, and by the ICREA Academia Programme. This research was funded by the National Institutes of Health, National Institute of General Medical Sciences Grant R01 GM088428 and the National Science Foundation Grant MCB-1450867 (both to G.M.S.)

Chapter 2: Species-independent attraction to biofilms through electrical signaling

Chapter 2.1 – Abstract

Bacteria residing within biofilm communities can coordinate their behavior through cell-to-cell signaling. However, it remains unclear if these signals can also influence the behavior of distant cells that are not part of the community. Using a microfluidic approach, we find that potassium ion channel-mediated electrical signaling generated by a *Bacillus subtilis* biofilm can attract distant cells. Integration of experiments and mathematical modeling indicates that extracellular potassium emitted from the biofilm alters the membrane potential of distant cells, thereby directing their motility. This electrically-mediated attraction appears to be a generic mechanism that enables cross-species interactions, as *Pseudomonas aeruginosa* cells also become attracted to the electrical signal released by the *B. subtilis* biofilm. Cells within a biofilm community can thus not only coordinate their own behavior, but also influence the behavior of diverse bacteria at a distance through long-range electrical signaling.

Chapter 2.2 – Introduction

Bacteria within biofilms can coordinate their behavior through distinct forms of communication (Shapiro 1998; Waters & Bassler 2005; Brameyer et al. 2015; Liu et al. 2015). The best characterized cell-to-cell signaling process in bacteria is known as quorum sensing (Miller & Bassler 2001). Recently another cell-to-cell communication mechanism based on ion channel-mediated electrical signaling has also been described (Prindle et al. 2015). This electrical signaling has been shown to facilitate communication within a biofilm community (Liu et al. 2015; Prindle et al. 2015). Specifically, cells within *B. subtilis* biofilms can actively relay extracellular potassium signals, producing electrical waves that propagate through the biofilm and coordinate metabolic states, thereby increasing collective fitness (Prindle et al. 2015; Liu et al. 2015). These findings provoke the question of whether such extracellular signals could extend beyond the biofilm, resulting in long-range interactions that could affect distant bacteria that are not part of the biofilm. Here we utilized a microfluidic approach to investigate whether electrical signals generated within the biofilm can influence the behavior of other bacteria that share the same aqueous environment. In particular, we hypothesized that electrical signals could direct bacterial motility through altering the membrane potential. Such long-range signaling could provide a generic mechanism for bacterial communities to exert control over the motile behavior of distant cells.

Chapter 2.3 - Periodic attraction of distant motile cells to electrically oscillating biofilms

We began by measuring the interaction dynamics between a biofilm and motile cells in a large microfluidic chamber (3 mm x 3 mm x 6 μm) (**Fig. S2.1**). Specifically, we grew a biofilm in the microfluidic chamber until it reached the size (over one million cells) at which oscillations emerge (Liu et al. 2015). We then introduced motile cells into the chamber and noticed that they were periodically attracted to the electrically oscillating biofilm. To accurately discriminate between biofilm and motile cells, we then introduced fluorescently labeled motile cells (constitutively expressing a fluorescent protein) into the growth chamber, again after biofilm formation (**Fig. 2.1a**). To determine the relationship between motile cell attraction and electrical oscillations in the biofilm (Prindle et al. 2015), we quantified the membrane potential of biofilm cells by using the previously characterized fluorescent cationic dye Thioflavin T (ThT) (**Fig. 2.1a**) (Prindle et al. 2015). This charged reporter dye diffuses across the membrane according to the membrane potential and thereby acts as a Nernstian voltage indicator of bacterial membrane potential (Plásek & Sigler 1996). This approach revealed that the periodic increase in motile cell density at the biofilm edge accurately tracks the oscillations in biofilm membrane potential (**Fig. 2.1b, c)**. In particular, the peak accumulation of motile cells at the biofilm edge slightly lags the peak of electrical signaling in the biofilm by 26 ± 9 min (mean $\pm$ st. dev., n = 44 pulses **Fig. 2.1c**, **d**). Furthermore, the period of motile cell attraction to the biofilm edge tracks with the natural variation in the period of electrical signaling within biofilms (**Fig. 2.1e**). We observed no attraction of motile cells to biofilms that had not yet initiated

electrical oscillations (**Fig. S2.2**), suggesting that electrical signaling plays a critical role in motile cell attraction. In addition, functional motility machinery in distant cells is also required, as non-motile cells lacking the flagellin gene *hag* showed no attraction to electrically oscillating biofilms (**Fig. 2.1f**). Together, these results show that electrical oscillations generated by the biofilm are correlated in time with periodic attraction of distant motile cells to the biofilm.

Chapter 2.4 - Sufficiency of extracellular potassium in directing cell motility

We next asked whether the observed attraction of motile cells was due to changes in extracellular potassium generated during biofilm oscillations (Prindle et al. 2015). Utilizing the microfluidic device, we directly tested whether potassium signals were sufficient to influence motile cells. Specifically, we investigated whether we could redirect motile cells away from the biofilm by providing an alternative and stronger source of extracellular potassium. Accordingly, we transiently flowed media supplemented with potassium into the region most distant from the biofilm (**Fig. 2.2a**). This alternative potassium source was introduced during a peak in biofilm electrical activity (maximal motile cell attraction) (**Fig. 2.2b**). We find that instead of being attracted to the biofilm, motile cells now accumulated at the competing potassium source (**Fig. 2.2b, c**). Removal of this alternative potassium source restored motile cell attraction to the biofilm in the subsequent pulse of electrical activity (**Fig. 2.2b**). These

results demonstrate that changes in extracellular potassium gradients are sufficient to direct motile cell behavior.

We then began to investigate the potential mechanism by which waves of extracellular potassium released by the biofilm could influence the motility of distant cells. It is known that changes in extracellular potassium lead to changes in the cell's membrane potential and proton motive force (Bakker & Mangerich 1981; Booth 1985; Abee et al. 1988). The proton motive force in turn influences bacterial motility by controlling the frequency of tumbling events that enable a biased random walk along a concentration gradient (Berg & Brown 1972; De Jong et al. 1976; Manson et al. 1977; Miller & Koshland 1980). The relationship between extracellular potassium, membrane potential and tumbling frequency of motile cells suggests a possible mechanism for the observed attraction of motile cells to biofilms.

Chapter 2.5 - The role of the potassium ion channel in motile cell attraction

To determine the mechanism of motile cell attraction, we first confirmed that potassium ion channel activity in the biofilm generates the extracellular potassium signal that results in motile cell attraction. Complete deletion of the potassium ion channel YugO interferes with *B. subtilis* biofilm formation (Lundberg et al. 2013; Prindle et al. 2015). Therefore, we turned to a previously characterized mutant strain (*ΔtrkA*), which only lacks the TrkA gating domain of the YugO potassium ion channel and exhibits diminished electrical signaling (Prindle et al. 2015) (**Fig. 2.3b**). We find that

biofilms formed by this mutant strain have a 75% ± 4% (mean ± st. dev., n = 3 experiments for each genotype) lower electrical signaling amplitude when compared to wild type biofilms (**Fig. 2.3a, b**). Correspondingly, motile cell attraction to *ΔtrkA* biofilms is reduced by 70% ± 9% (mean ± st. dev., n = 3 experiments for each genotype) (**Fig. 2.3d**). Therefore, we find a direct correlation between the weaker electrical signal generated by *ΔtrkA* biofilms and the corresponding decrease in motile cell attraction. These results show that potassium ion channels in biofilm cells play an important role in generating the electrical signal that attracts motile cells.

Chapter 2.6 - Motile cell membrane potential influences attraction to biofilms

We speculated that attraction of motile cells depends not only on the signal emitted by the biofilm, but also the sensitivity of motile cells to the potassium signal. Specifically, the sensitivity to changes in extracellular potassium depends on the resting membrane potential of the cell (Hille 2001).We anticipated that motile cells with a more negative resting membrane potential would be more sensitive to the potassium signals emitted by the biofilm. Accordingly, we deleted the major *B. subtilis* potassium pump (KtrA) in motile cells. Potassium pumps are responsible for maintaining the high intracellular concentration of potassium ions and thus play a key role in establishing the resting membrane potential (Castañeda-García et al. 2011; Gries et al. 2013). Consequently, *ΔktrA* motile cells would have a reduced ability to pump in positively charged potassium ions and thus have a relatively more negative

membrane potential. Indeed, we find a 57% ± 6% (st. dev., n = 2 experiments) more negative membrane potential in the *ΔktrA* strain relative to wild type (**Figure S2.3**). When exposed to wild type biofilms with nearly identical electrical oscillation amplitudes, we observed more than two-fold (239% ± 25%, st. dev., n = 8 experiments) increase in attraction of *ΔktrA* motile cells, compared to wild-type motile cells (**Fig. 2.3 a, c, d**). These results show that attraction also depends on the membrane potential-mediated sensitivity of motile cells to the potassium signals generated by the biofilm.

Chapter 2.7 - Membrane potential and tumbling frequency of distant cells depend on biofilm oscillations

Next, we established that electrical activity within the biofilm can alter the membrane potential of distant cells. We confirmed that an electrically active biofilm generates a dynamic potassium gradient, as reported by the potassium specific fluorescent dye Asante Potassium Green 4 (APG-4) (**Fig. 2.4a, S2.4**). We then utilized distant cells that by chance adhered to the microfluidic chamber to measure membrane potential in individual cells over time without having to track their movement (**Fig. 2.4b**). This allowed us to precisely measure the membrane potential dynamics of distant cells during an entire period of electrical signaling in the biofilm. We find that the membrane potential of these stationary cells becomes more negative during the peak of electrical oscillations in the biofilm (**Fig. 2.4c, d**). Together, these

data indicate that potassium waves generated by the biofilm can induce changes in the membrane potential of distant cells.

We then asked whether the tumbling frequency of individual motile cells also depends on the electrical activity of the biofilm. Using phase contrast imaging every 10 msec, we compared a total of 2,668 motile cell trajectories obtained specifically during a peak or trough of electrical oscillations in the biofilm (**Figure 2.4e**). This approach allowed us to determine the relationship between tumbling frequency of motile cells and the electrical signaling generated by the biofilm. During the peak of electrical activity in the biofilm, we observed that the tumbling frequency of motile cells was inversely related to their distance from the biofilm (**Figure 2.4f**). In other words, distant motile cells exhibited directional swimming, while cells already near the electrically active biofilm edge tumbled and thus remained at the biofilm edge. In contrast, there was no such spatial organization of tumbling frequencies during the trough in biofilm electrical activity (**Figure 2.4f**). These results suggest that the tumbling frequency of motile cells is altered by the spatio-temporal extracellular potassium gradient generated by the biofilm.

Chapter 2.8 - Agent-based mathematical modeling confirms that extracellular potassium can direct motility

To integrate the above described multiple lines of experimental evidence into a coherent phenomenological framework, we turned to mathematical modeling. We

utilized an electrophysiological model based on the mathematical framework developed by Hodgkin and Huxley to predict changes in membrane potential in response to extracellular potassium (Prindle et al. 2015; Hodgkin & Huxley 1952) (see **Methods** for details). This model was constrained by our measurement of membrane potential dynamics observed in distant stationary cells (**Fig. 2.4d**). We integrated this electrophysiological model with an agent-based physical model (Mather et al. 2010; Volfson et al. 2008) to simulate the motility of individual cells (see **Methods** for details of the agent-based model). In brief, cells were modeled as soft spherocylinders that moved according to Newton's law under the forces and torques caused by their own motility and contacts with other cells. In a departure from earlier models (Prindle et al. 2015; Mather et al. 2010; Volfson et al. 2008), each cell was endowed with a set of ordinary differential equations coupling its electrophysiological state with its motility (**Fig. 2.5a, Methods**). Using this model, we computed how a change in extracellular potassium altered the cell's membrane potential and how this in turn affected the tumbling probability of each motile cell (**Fig. 2.5a, Fig. S2.5**) (De Jong et al. 1976; Manson et al. 1977; Miller & Koshland 1980). Furthermore, the simulations contained non-motile biofilm cells that were assumed to alternate between acting as a source or sink of potassium (peak and trough electrical activity respectively) (**Fig. 2.5b**, cyan and black cells, respectively). The resulting extracellular potassium dynamics followed the standard diffusion equation (see **Methods** for details). Consistent with experimental results, simulations showed periodic attraction of distant motile cells to an electrically

oscillating biofilm (**Fig. 2.5b**). These modeling results demonstrate that an oscillating source (biofilm) of extracellular potassium can periodically attract motile cells by changing their membrane potential.

Our model was predominantly informed by measurements in stationary cells, providing the opportunity to independently validate modeling predictions through additional motile cell measurements. In particular, we tested the modeling prediction that motile cells moving along a spatial potassium gradient are expected to have a similar membrane potential profile as stationary cells responding to temporal changes of potassium (**Fig. 2.5c**). In other words, motile cells during peak biofilm electrical activity should on average have a more negative membrane potential. To test this prediction, we measured the distribution of membrane potential in motile cells specifically at the attraction (peak) and non-attraction (trough) phases of the electrical oscillations in the biofilm. As predicted by our model, we find that motile cells have on average a more negative membrane potential in the attraction phase (**Fig. 2.5d**). These data show that similar to stationary cells, the membrane potential of motile cells also depends on the electrical activity of the biofilm. In addition, we find that the motile cell density profile as a function of time and distance from the biofilm is consistent with modeling predictions (**Fig. 2.5e, f**). Together, these results further validate the mathematical model and allow us to establish a coherent framework to interpret experimental observations.

Chapter 2.9 - Electrically mediated attraction applies across distinct bacterial species

The membrane potential plays a general role in bacterial motility (Manson et al. 1977; Meister et al. 1987; Lo et al. 2007), and thus a mechanism of attraction based on inducing changes in membrane potential could apply to other bacterial species as well. To test this hypothesis, we studied the interaction of *Pseudomonas aeruginosa* cells with a pre-existing *B. subtilis* biofilm. We chose *P. aeruginosa* because it is a Gram-negative bacterium that is evolutionarily distant to Gram-positive *B. subtilis*. As expected, we find that motile *P. aeruginosa* cells also become periodically attracted to the *B. subtilis* biofilm during electrical oscillations (**Fig. 2.6a, b, S6**). Consistent with observations for *B. subtilis*, we find that the peak accumulation of *P. aeruginosa* motile cells at the biofilm edge again lags the peak of electrical activity in the biofilm by 22 $\pm$ 13 min (mean $\pm$ st. dev., n = 30 pulses) (**Fig. 2.6c**). In addition, variations in the period of electrical signaling within the biofilm are directly matched by the period of *P. aeruginosa* attraction to the biofilm edge (**Fig. 2.6d**). These results indicate that the mechanism of electrically-mediated attraction is not limited to *B. subtilis* cells, and thus enables cross-species interactions.

Chapter 2.10 - Strength of electrical attraction modulates incorporation of new members into a biofilm

Attraction of distant cells to the biofilm edge could result in their incorporation into the biofilm, providing an additional opportunity to quantify the strength of

electrical attraction (**Fig. 2.7a**). We first confirmed that motile *B. subtilis* cells can become permanently incorporated into a pre-existing *B. subtilis* biofilm by utilizing the fluorescence labeling of motile cells (**Fig. 2.7b**). We then utilized Δ*trkA* mutant biofilms that are deficient in electrical attraction to determine if reduced electrical attraction would decrease incorporation of distant cells into the biofilm. As expected, we find less permanent incorporation of *B. subtilis* cells into Δ*trkA* mutant biofilms (**Fig. 2.7c**). Importantly, we find that *P. aeruginosa* cells can also become permanently incorporated into a *B. subtilis* biofilm. Consistent with *B. subtilis* motile cell results, we find less incorporation of *P. aeruginosa* motile cells into Δ*trkA B. subtilis* biofilms (**Fig. 2.7d, e**). The strong correlation between motile cell attraction and permanent incorporation for both species confirms that incorporation accurately reflects the strength of motile cell attraction (**Fig. 2.7f, g**). These data show that the level of permanent incorporation of new members into a pre-existing biofilm depends on the strength of electrical attraction.

Chapter 2.11 - Discussion

Our study shows that electrical signaling mediated by potassium ion channels can extend beyond the boundaries of a biofilm to attract distant cells. This attraction is driven by dynamic gradients of potassium ions, which can alter the membrane potential of distant cells and thereby direct their motile behavior. Our work thus builds on and extends previous studies that emphasize the importance of membrane

potential in bacterial motility (Miller & Koshland 1977; Manson et al. 1977; Shioi et al. 1978; Matsuura et al. 1979; Miller & Koshland 1980; Shioi et al. 1980; Meister et al. 1987; Meister et al. 1989; Lo et al. 2007). We find that long-range signaling mediated through potassium ions can generate a rapid response in cell motility, because it does not require biochemical synthesis or complex signaling networks. Given our experimental conditions, bacterial communities can effectively modulate the motility of distant cells through potassium ion channel-mediated electrical signals. These results indicate that bacterial biofilms not only regulate the behavior of cells that reside within the community, but also exert control over distant cells that are not part of the community.

Our findings show that the interaction mechanism between the biofilm and distant cells applies to even evolutionarily distant bacteria and is thus not limited to cells from a single species. In particular, the effect of extracellular potassium on membrane potential is shared among all cells, because the interaction is of physical nature. This suggests a new paradigm for long-range cross-species signaling that is generic, as it does not require specific receptors or signaling pathways. Interestingly, as a result of cross-species attraction, bacteria from a different species can become incorporated into a preexisting biofilm. Therefore, our work raises many new intriguing questions regarding the complex co-existence of biofilm communities and surrounding cells. The pursuit of these questions is likely to provide not only basic insights, but also

tools that can be utilized in synthetic biology approaches to control the interaction of single cells and communities.

Chapter 2.12 – Figures

Figure 2.1. Distant motile cells are periodically attracted to an electrically oscillating biofilm. **a,** Illustration of motile cell interaction with a biofilm within a shared microfluidic growth chamber (see **Figure S2.1**). Media flows in the direction indicated by the gray arrow, at a rate of 12 μm/s. Membrane potential changes are reported by Thioflavin T (ThT, pseudocolored cyan), a cationic dye that acts as a Nernstian voltage indicator (Prindle et al. 2015). ThT fluorescence increases when the cell becomes more inside-negative, making ThT fluorescence inversely related to the membrane potential. Motile cells (pseudocolored red) express a fluorescent protein mKate2 from the $P_{hyperspank}$ promoter induced with 1 mM IPTG. Motile cell density is measured using mKate2 fluorescence (only present in motile cells) in the 100 μm region outward from the biofilm edge (indicated as a solid white line). Scale bar, 50 μm. **b,** Filmstrip showing the edge of a biofilm which is located on the top of each image. Images depict periodic motile cell attraction to an electrically oscillating biofilm and subsequent passive dispersal away from the biofilm. Gray (phase contrast), cyan (membrane potential), red (motile cells). Scale bar, 50 μm. **c,** Time series of motile cell density (red) near the biofilm edge together with membrane potential reporter ThT measured within the biofilm (cyan). Time series shows that motile cell density changes periodically along with electrical oscillations within the biofilm. Time series is representative of 3 independently reproduced experiments. **d,** Histogram of the time between peaks in biofilm electrical activity and peaks in motile cell attraction (motile cell density lag). Motile cell peaks occur on average 26.4 ± 8.8 min after the initiation of electrical oscillations within the biofilm (mean ± st. dev., n = 44 pulses). Inset, illustration of the quantification method for motile cell density lag. Motile cell density lag is defined as the time between the electrical pulse (cyan) and the motile cell pulse (red), represented with an arrow. **e,** Scatter plot of the periods of electrical oscillations within biofilms (peak to peak) and the periods of co-occurring pulses in motile cell attraction (peak to peak). Periods of motile cell attraction correlate with natural variations in the periods of electrical oscillations within biofilms (Pearson correlation coefficient = 0.96, n = 33 periods). **f,** Time series of non-motile (Δ*hag,* red) cell density together with biofilm membrane potential (cyan). Time series shows no periodic attraction of non-motile cells to an oscillating biofilm. Time series is representative of 3 independently reproduced experiments. See also **Figure S2.2**.

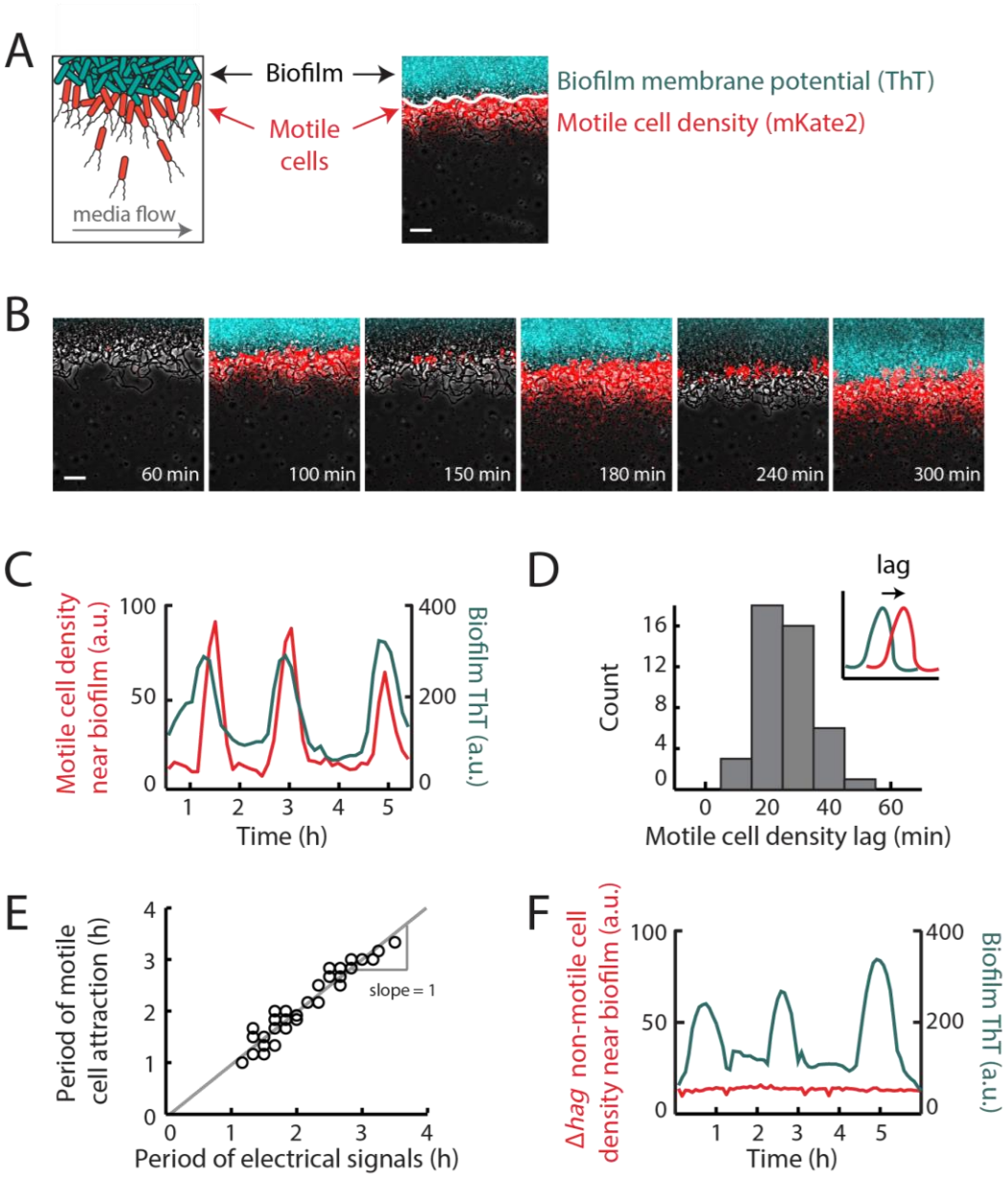
A
Biofilm
Motile cells
media flow
Biofilm membrane potential (ThT)
Motile cell density (mKate2)
B
60 min
100 min
150 min
180 min
240 min
300 min
C
Motile cell density near biofilm (a.u.)
Biofilm ThT (a.u.)
Time (h)
D
lag
Count
Motile cell density lag (min)
E
Period of motile cell attraction (h)
slope = 1
Period of electrical signals (h)
F
Δhag non-motile cell density near biofilm (a.u.)
Biofilm ThT (a.u.)
Time (h)

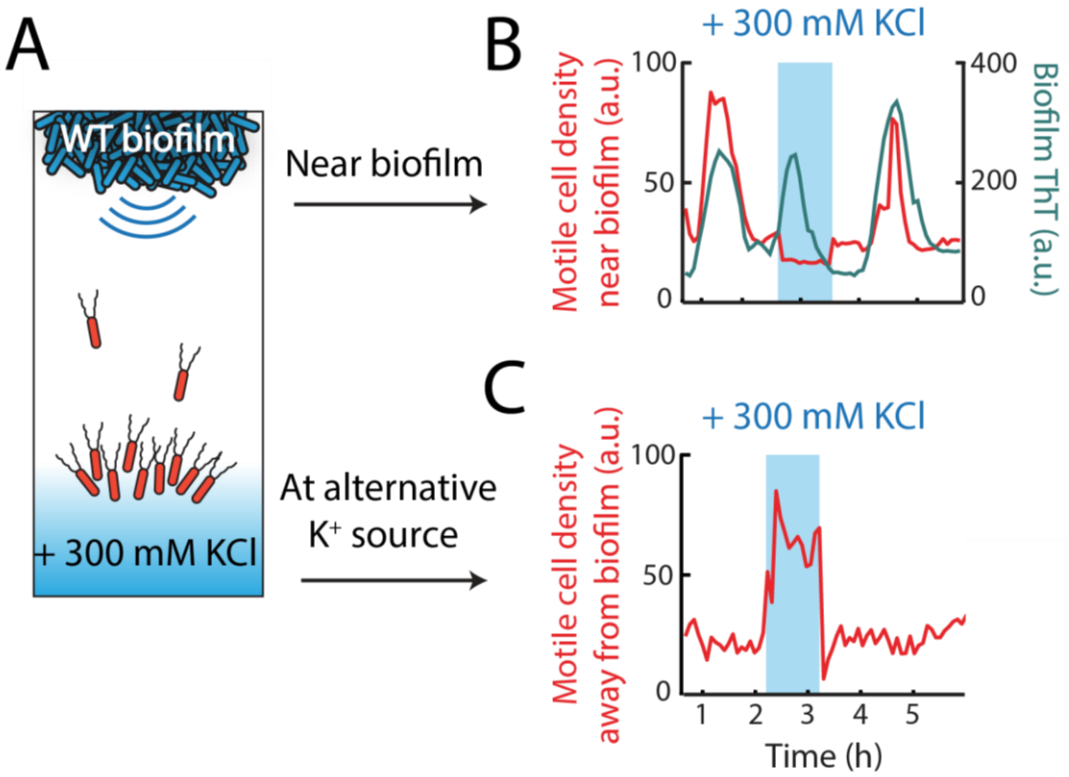

Figure 2.2. Extracellular potassium is sufficient to direct motility. **a,** An alternative potassium source is introduced into the growth chamber (blue shading) to redirect motile cells away from an oscillating biofilm. Arrows indicate the two regions where cell density was evaluated for the time series shown in (b, c). **b, c,** Time series showing redirection of motile cells (in red) away from the electrically oscillating biofilm (shown in (b), cyan) and towards the alternative potassium source (MSgg + 300 mM KCl, shown in (c)) which was introduced at a distance from the biofilm edge. The alternative potassium source (indicated by blue shading) was generated for 1 hour during the peak of electrical activity in the biofilm when motile cell attraction is typically maximal. Time series shown are representative of 8 independently reproduced experiments.

Figure 2.3. Motile cell attraction depends both on the strength of biofilm electrical signals and the sensitivity of motile cells to these signals. **a,** (Top) wild type cells contain a potassium ion channel YugO that is gated by a TrkA domain, and a potassium ion pump KtrA. (Bottom) Wild type (WT) motile cell attraction (in red) to electrical oscillations from a WT biofilm (in cyan, same data as **Figure 2.1**, shown here for comparison to (b) and (c)). **b,** (top) The TrkA gating domain of YugO was deleted in biofilm cells, resulting in reduced biofilm signaling. (bottom) Time series of WT motile cell response to *ΔtrkA* biofilm electrical oscillations shows reduced oscillation amplitude (n = 6, $p = 2.20 \times 10^{-7}$, two sample t-test), and reduced motile cell attraction compared to a WT biofilm (n = 3, $p = 2.24 \times 10^{-7}$, two sample t-test). Time series is representative of 6 independently reproduced experiments. **c,** (top) The potassium pump KtrA was deleted in motile cells, which leads to hyperpolarization (See **Figure S2.3**) and increased sensitivity to potassium signals. (bottom) Time series of Δ*ktrA* motile cell response to WT biofilm electrical oscillations shows increased attraction (n = 8, $p = 6.66 \times 10^{-6}$, two sample t-test) compared to WT motile cells responding to a WT biofilm (see (a)). WT biofilms in this experiment had similar oscillation amplitude as in (a) (n = 3, p = 0.906, two sample t-test). Time series is representative of 8 independently reproduced experiments. **d,** Plot of average peak biofilm signal vs. average peak motile cell response for WT (gray circle) compared to Δ*trkA* (purple circle) and Δ*ktrA* (yellow circle) mutants shows that reducing the amplitude of the potassium signal reduces attraction, while increasing the sensitivity to the potassium signal increases attraction (mean ± st. dev., WT n = 3, Δ*trkA* n = 6, Δ*ktrA* n = 8).

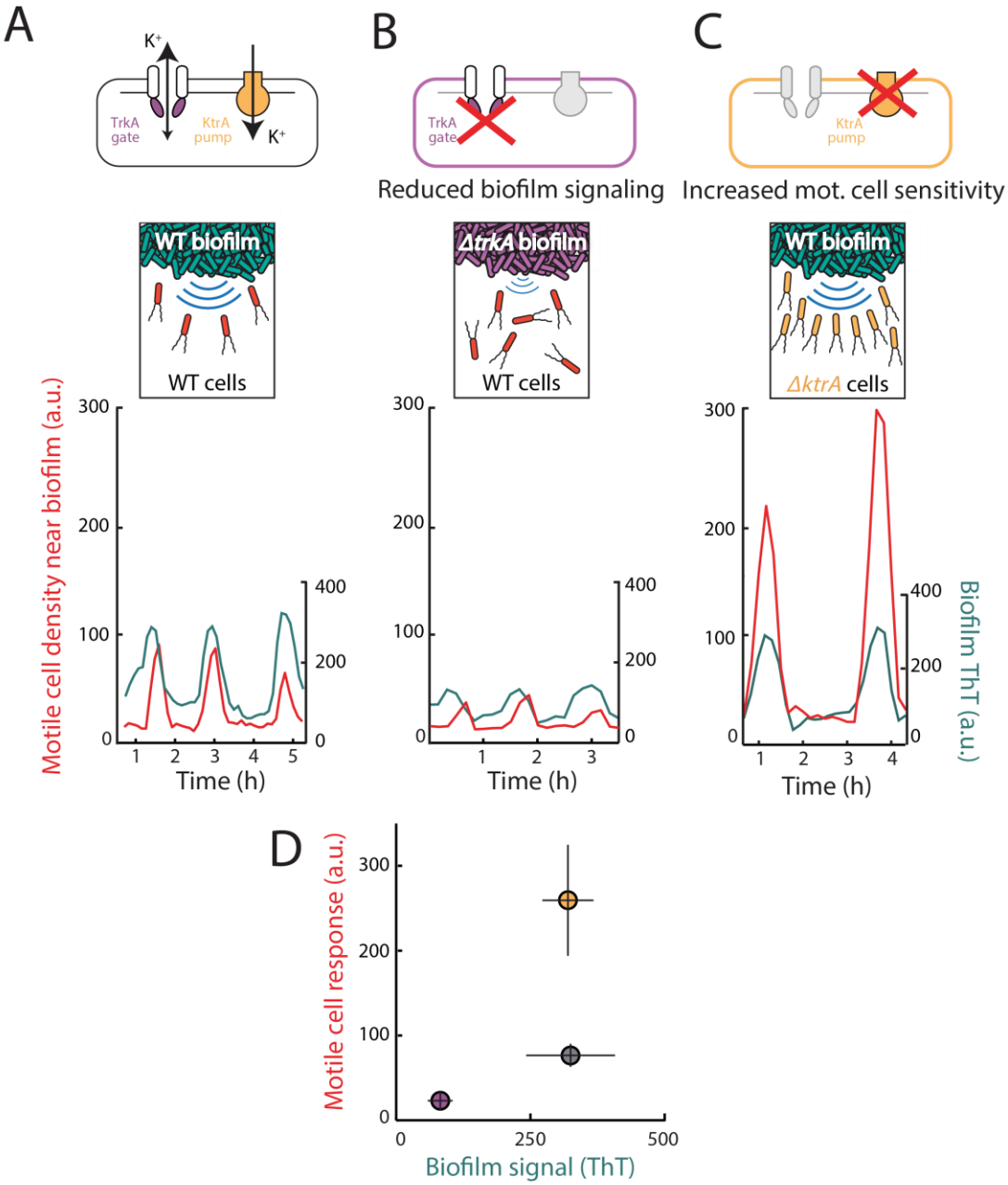
A
K+
TrkA gate
KtrA pump
K+
B
TrkA gate
Reduced biofilm signaling
C
KtrA pump
Increased mot. cell sensitivity
WT biofilm
WT cells
ΔtrkA biofilm
WT cells
WT biofilm
ΔktrA cells
Motile cell density near biofilm (a.u.)
Biofilm ThT (a.u.)
Time (h)
Time (h)
Time (h)
D
Motile cell response (a.u.)
Biofilm signal (ThT)

Figure 2.4. Extracellular potassium is a long range signal that can influence the membrane potential and tumbling frequency of motile cells. **a,** The fluorescent chemical dye Asante Potassium Green (APG-4) was used to track the extracellular concentration of potassium between cells in the biofilm and the surrounding cell free region. APG-4 fluorescence was measured over time at the regions shown in the phase image on the left. On the right, time series of APG-4 fluorescence intensity oscillations between cells in the biofilm (top), and in the cell-free region distant from the biofilm (bottom). Scale bar, 50 μm. See also **Figure S2.4**. **b,** Phase contrast image of a biofilm and distant stationary cells. The membrane potential of cells circled in black was tracked over time to determine the response to long-range signals emitted from the biofilm. Scale bar, 12 μm. **c,** Time series of a membrane potential (ThT) pulse in the biofilm. **d,** Time series of the co-occurring membrane potential pulse in distant cells shows membrane potential changes that are in phase with biofilm electrical oscillations. **e,** Individual motile cells were tracked over time and their motion was compiled into trajectories that trace their movement. To track motile cells, we used high frequency (10 msec interval) phase contrast imaging. Sample trajectories are shown for 3 different average tumbling frequencies and are colored based on their average tumbling frequency (1/s), color scale is the same as in (f). **f,** Individual motile cells were tracked near the biofilm at both the peak and trough of electrical activity (n = 2,668 trajectories). Trajectories are colored based on their average tumbling frequency, and overlaid on a phase contrast image of the biofilm. (left) During a peak in electrical activity in the biofilm, motile cell tumbling frequencies are inversely related to distance from the biofilm, consistent with a biased random walk up a potassium concentration gradient. (right) During a trough in biofilm electrical activity, there is no relationship between motile cell tumbling frequency and distance from the biofilm. The biofilm is at the top of each image, scale bar applies to both images. Overlaid trajectories include cells which were tracked for at least 500 ms.

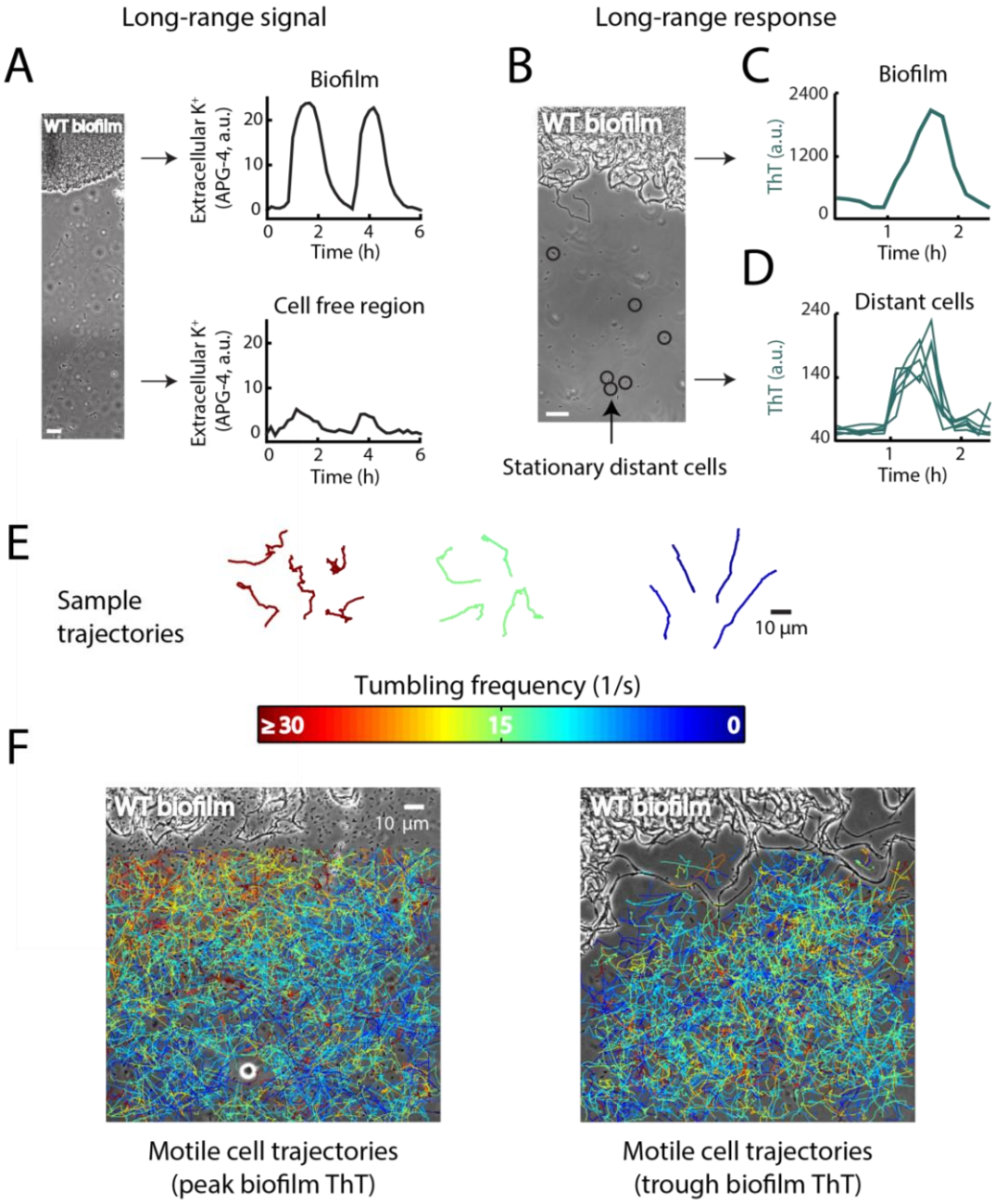
Long-range signal
Long-range response
A
B
C
D
E
F
WT biofilm
Biofilm
Extracellular K+ (APG-4, a.u.)
Time (h)
Cell free region
ThT (a.u.)
Distant cells
Stationary distant cells
Sample trajectories
10 µm
Tumbling frequency (1/s)
≥ 30
15
0
Motile cell trajectories (peak biofilm ThT)
Motile cell trajectories (trough biofilm ThT)

Figure 2.5. Agent-based modeling of motile cell attraction driven by electrical signaling from biofilms. **a,** (top) Schematic illustrating how extracellular potassium alters motility by changing the membrane potential. Step 1: Extracellular potassium depolarizes the cell. Step 2: Depolarization prompts adaptation by the cell leading to hyperpolarization. Step 3: Hyperpolarization increases the proton motive force, thus directing motility by altering the tumbling frequency of the cell. (bottom) The computational model encompassing: (1) spatiotemporal reaction-diffusion model for the extracellular potassium K_e dynamics; (2) intracellular electrophysiological model for the cell membrane potential V, ion channel state n, metabolic stress S, intracellular potassium K_i and energy needed to drive the flagellar motor E (we can think of this energy as PMF or ATP); (3) discrete biomechanical model for individual cell motion influenced by their internal motility and interaction with other cells. The motility of individual cells is affected by the internal cellular state E via the change of the probability of tumbling $\mathcal{P}$. The details of the model and the model parameters are given in the **Methods**. See also **Figure S2.5**. **b,** Two snapshots of the combined agent-based simulation show increased density of motile (red) cells near the biofilm during the peak of the attraction phase to the biofilm. Biofilm cells are colored according to their membrane potential during each time point, where cyan coloring indicates more negative membrane potential relative to black coloring. **c,** Distributions of membrane potential in motile cells from the computational model indicate that motile cell membrane potential is more negative during the peak of the attraction phase to the biofilm. **d,** Experimental data confirms the modeling prediction that the distribution of motile cell membrane potential (ThT, a.u.) is relatively more negative during attraction to the biofilm compared to the non-attraction. **e,** Plot of motile cell density in the first 40 μm away from the biofilm edge over time, obtained from agent-based modeling simulations of motile cell attraction. The region closest to the biofilm edge is located at the top of the plots for both (e) and (f), and distance from the biofilm edge increases moving downward. **f,** Experimental data shows similar motile cell density dynamics in the first 40 μm away from the biofilm edge.

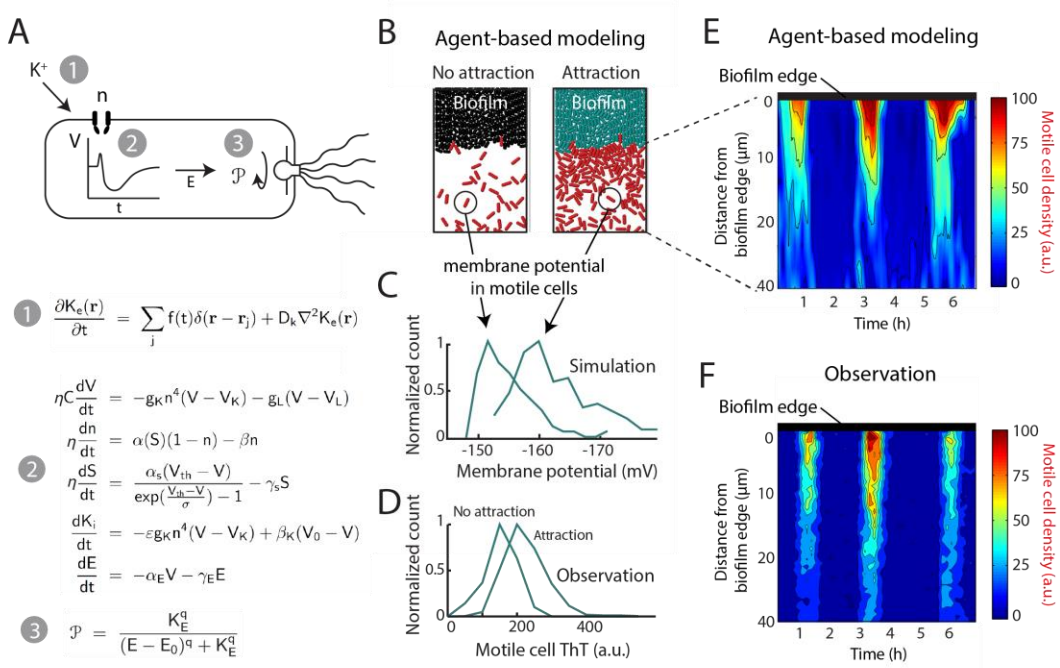

$$1 \quad \frac{\partial K_e(\mathbf{r})}{\partial t} = \sum_j f(t)\delta(\mathbf{r}-\mathbf{r}_j) + D_k \nabla^2 K_e(\mathbf{r})$$

$$2 \quad \begin{aligned} \eta C \frac{dV}{dt} &= -g_K n^4 (V - V_K) - g_L (V - V_L) \\ \eta \frac{dn}{dt} &= \alpha(S)(1-n) - \beta n \\ \eta \frac{dS}{dt} &= \frac{\alpha_s (V_{th} - V)}{\exp(\frac{V_{th}-V}{\sigma}) - 1} - \gamma_s S \\ \frac{dK_i}{dt} &= -\varepsilon g_K n^4 (V - V_K) + \beta_K (V_0 - V) \\ \frac{dE}{dt} &= -\alpha_E V - \gamma_E E \end{aligned}$$

$$3 \quad \mathcal{P} = \frac{K_E^q}{(E - E_0)^q + K_E^q}$$

Figure 2.6. Biofilm electrical signals can also attract other bacterial species. **a,** Film strip showing *P. aeruginosa* motile cell attraction to a pre-existing *B. subtilis* biofilm. Gray (phase contrast), cyan (membrane potential), green (*P. aeruginosa* motile cells). White line indicates the edge of the biofilm. Scale bar, 50 μm. **b,** Time series of *P. aeruginosa* motile cell accumulation (in green) near a *B. subtilis* biofilm, in phase with biofilm electrical oscillations (in cyan). Images and time series are representative of 12 independently reproduced experiments. **c,** Histogram of the time between peaks in biofilm electrical activity and peaks in *P. aeruginosa* motile cell attraction (motile cell density lag). Peaks in *P. aeruginosa* motile cell density occur on average 21.6 ± 13.4 min after the initiation of electrical oscillations within *B. subtilis* biofilms (mean ± st. dev., n = 30 pulses). (inset) Plot of the phase shift between peaks in *P. aeruginosa* attraction and *B. subtilis* electrical activity relative to the period of biofilm electrical oscillations. Arrows illustrate that a positive phase shift indicates a lag between a peak in *P. aeruginosa* attraction and biofilm electrical activity. **d,** Scatter plot of the periods of electrical oscillations within *B. subtilis* biofilms (peak to peak), and the periods of co-occurring pulses in *P. aeruginosa* motile cell attraction (peak to peak). The periods of pulses in motile cell density correlate with natural variations in the periods of electrical oscillations within biofilms (Pearson correlation coefficent = 0.83, n = 16 periods). See also **Figure S2.6**.

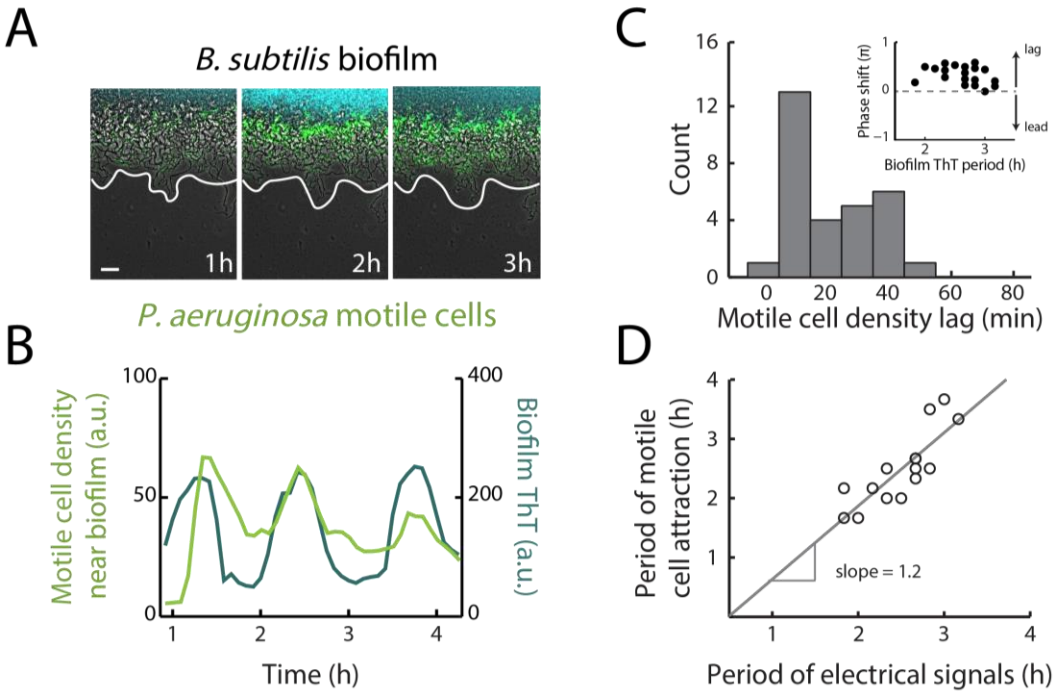
A
B. subtilis biofilm
1h
2h
3h
P. aeruginosa motile cells
B
Motile cell density near biofilm (a.u.)
Biofilm ThT (a.u.)
Time (h)
C
Count
Motile cell density lag (min)
Phase shift (π)
lag
lead
Biofilm ThT period (h)
D
Period of motile cell attraction (h)
slope = 1.2
Period of electrical signals (h)

Figure 2.7. Attraction can lead to incorporation of motile cells into biofilms, depending on the strength of the attraction. **a,** Illustration of how attraction can lead to incorporation of new cells into a pre-existing biofilm. Attracted cells (left panel) can remain attached to the biofilm following attraction (middle panel). Subsequent growth of the biofilm leads to capture of attached cells, resulting in permanent incorporation (right panel). **b,** Image of previously attracted *B. subtilis* motile cells (red) that have been incorporated into a pre-existing wild type *B. subtilis* biofilm. Image representative of 6 independently reproduced experiments. Incorporated cells are surrounded by cells originating from the pre-existing biofilm and are located inside the biofilm. **c,** Image of previously attracted *B. subtilis* motile cells that have been incorporated into a pre-existing *ΔtrkA* biofilm. Reduced *B. subtilis* motile cell attraction to *ΔtrkA* biofilms that are deficient in electrical signaling results in diminished incorporation into the biofilm. Image representative of 6 independently reproduced experiments. **d,** Image of previously attracted *P. aeruginosa* motile cells that also became incorporated into a pre-existing *B. subtilis* biofilm. Image representative of 12 independently reproduced experiments. **e,** Image of previously attracted *P.* aeruginosa motile cells that have become incorporated into a pre-existing *B. subtilis ΔtrkA* biofilm. Diminished incorporation of *P. aeruginosa* motile cells is also observed as a consequence of reduced attraction to *ΔtrkA B. subtilis* biofilms. Image representative of 5 independently reproduced experiments. **b, c, d, e,** White lines indicate each biofilm edge, and biofilms are located at the top of each image. Gray (phase contrast), red (*B. subtilis* motile cells), green (*P. aeruginosa* motile cells). Scale bars, 50 μm. **f, g,** Scatter plots comparing the average peak motile cell density during attraction to biofilms and the resulting permanent incorporation of these attracted cells into biofilms. The observed direct relationship indicates that the incorporation of attracted motile cells depends on the degree of attraction. **f,** Circles, *B. subtilis* motile cell attraction and incorporation into wild type *B. subtilis* biofilms (n = 6 independently reproduced experiments); squares, *B. subtilis* motile cells attraction and incorporation into electrical signaling deficient *ΔtrkA B. subtilis* biofilms (Pearson correlation coefficient = 0.98, n = 3 independently reproduced experiments). **g,** Circles, *P. aeruginosa* motile cell attraction and incorporation into wild type *B. subtilis* biofilms (n = 6 independently reproduced experiments); squares, *P. aeruginosa* motile cell attraction and incorporation into signaling deficient *ΔtrkA B. subtilis* biofilms (Pearson correlation coefficient = 0.91, n = 5 independently reproduced experiments).

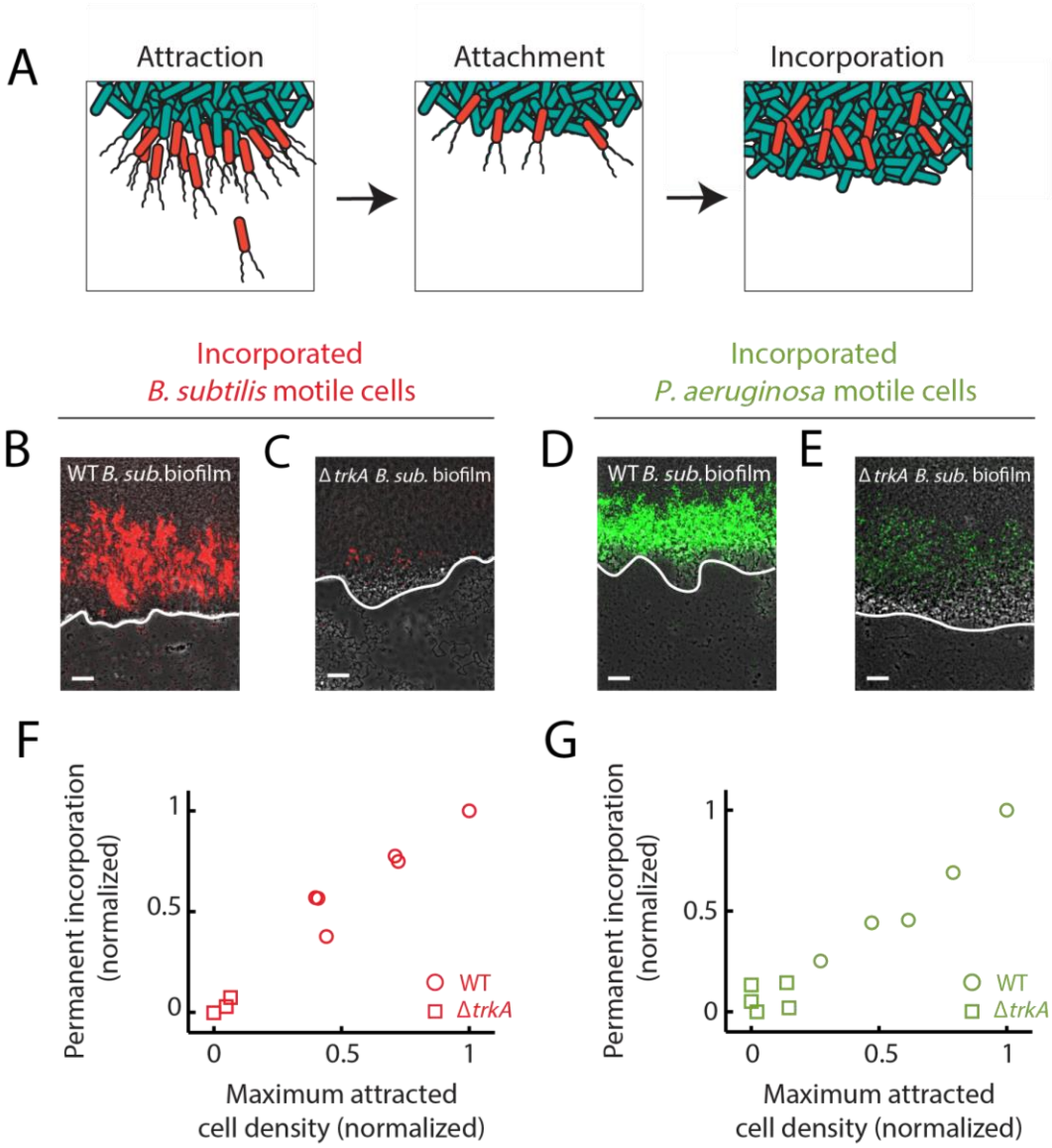
A
Attraction
Attachment
Incorporation
Incorporated
B. subtilis motile cells
Incorporated
P. aeruginosa motile cells
B
WT B. sub. biofilm
C
Δ trkA B. sub. biofilm
D
WT B. sub. biofilm
E
Δ trkA B. sub. biofilm
F
Permanent incorporation (normalized)
Maximum attracted cell density (normalized)
WT
ΔtrkA
G
Permanent incorporation (normalized)
Maximum attracted cell density (normalized)
WT
ΔtrkA

Chapter 2.13 - Supplemental figures

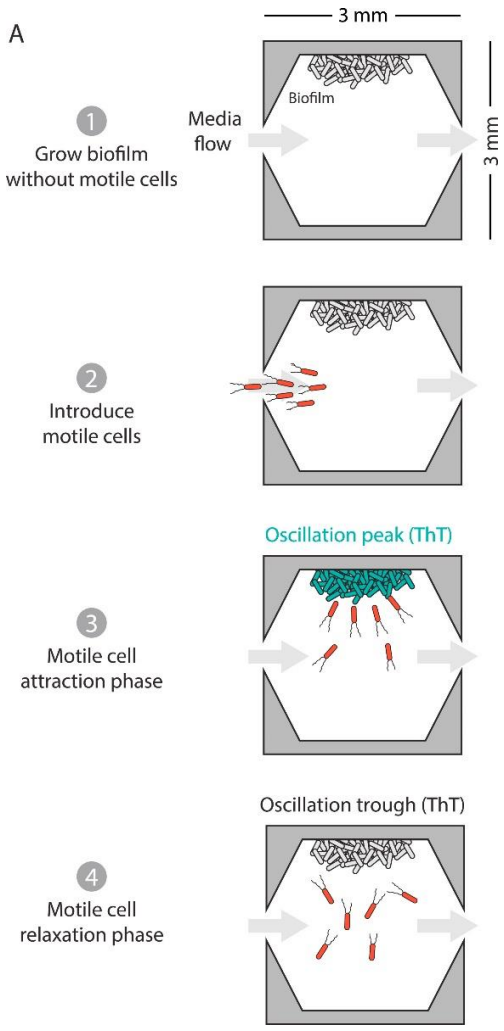

Figure S2.1. Outline of the experimental procedure used to measure the interaction dynamics between biofilms and motile cells. The microfluidic device used in our experiments has a growth chamber that measures 3mm x 3mm x 6 µm (X x Y x Z). Biofilms grow from a side wall outward as illustrated, and media flows through the device at a rate of 12 µm/s. Step 1, grow biofilm without motile cells until it reaches critical size for oscillations. Step 2, introduce motile cells into growth chamber with the biofilm. Step 3-4, as oscillations occur, we image biofilm electrical oscillations with the fluorescent membrane potential reporter Thioflavin T (ThT) and motile cell movement with a fluorescent constitutive reporter *Phyp-mKate2*. Depending on the phase of oscillations (peak or trough), we see periodic attraction of motile cells toward the biofilm.

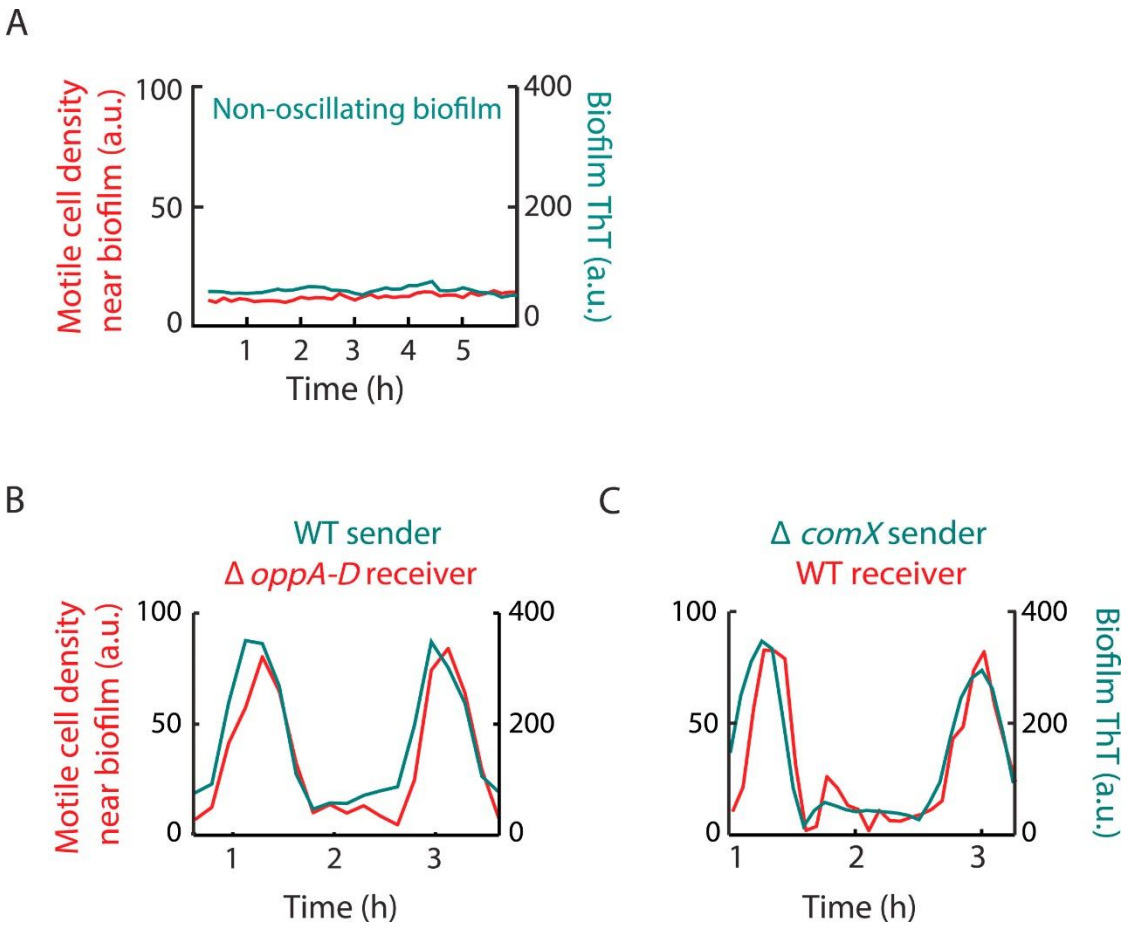

Figure S2.2. a, Time series of motile cell density near a biofilm that has not yet initiated electrical oscillations, and corresponding membrane potential in the biofilm. Motile cells fail to respond to a biofilm that has not yet initiated electrical oscillations. Time series is representative of 3 independently reproduced experiments. **b,** Time series of *ΔoppA-D* motile cells (receivers) responding to a wild type biofilm (sender). The *oppA-D* operon encodes the transporter required for the uptake of the major quorum-sensing peptide family (*phr*) (Perego et al. 1991), and we observed no effect of this deletion on motile cell attraction. **c,** Time series of wild type motile cells responding to a *ΔcomX* biofilm also shows no effect on motile cell attraction. The *comX* gene encodes one of the best characterized quorum-sensing signaling peptides (Magnuson et al. 1994), and we again observed no effect of this deletion on motile cell attraction.

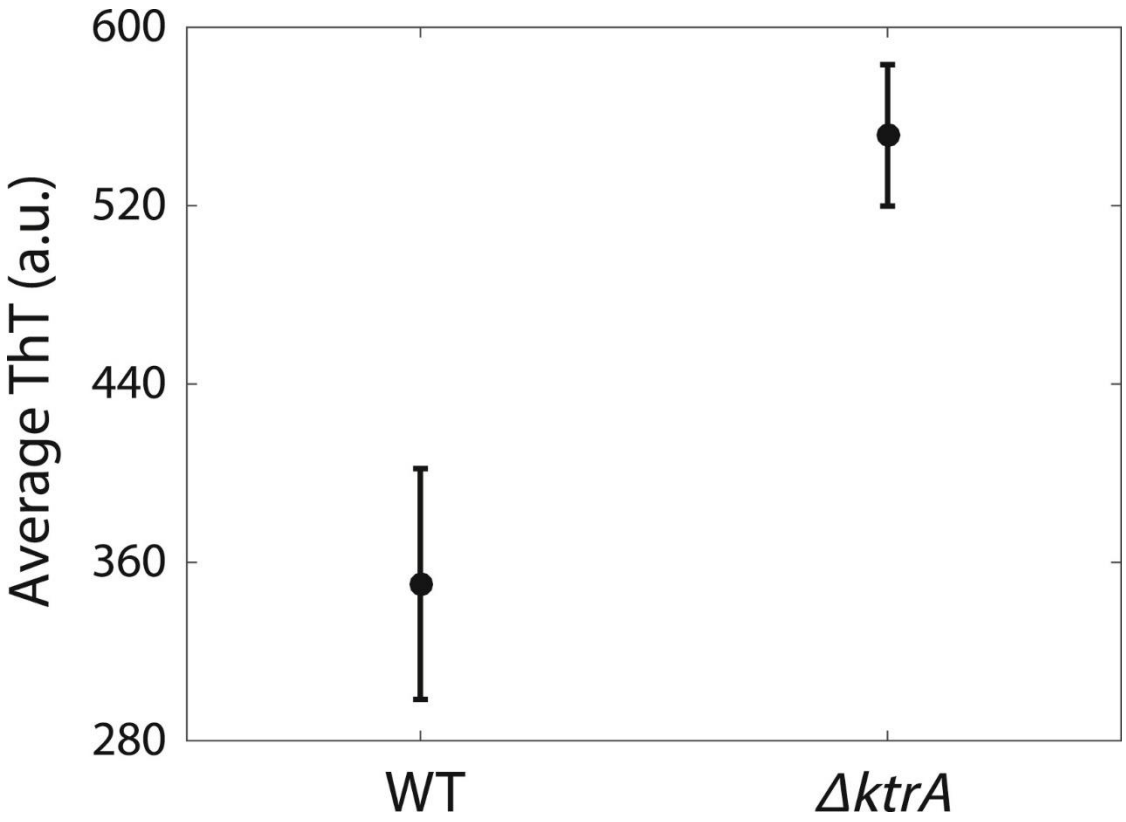

Figure S2.3. Deletion of the KtrA potassium pump in *B. subtilis* results in hyperpolarization of membrane potential. Plot of average ThT in wild type (WT) and *ΔktrA* cells (n = 2 *ΔktrA* biofilms, 1 WT biofilm ± st. dev.).

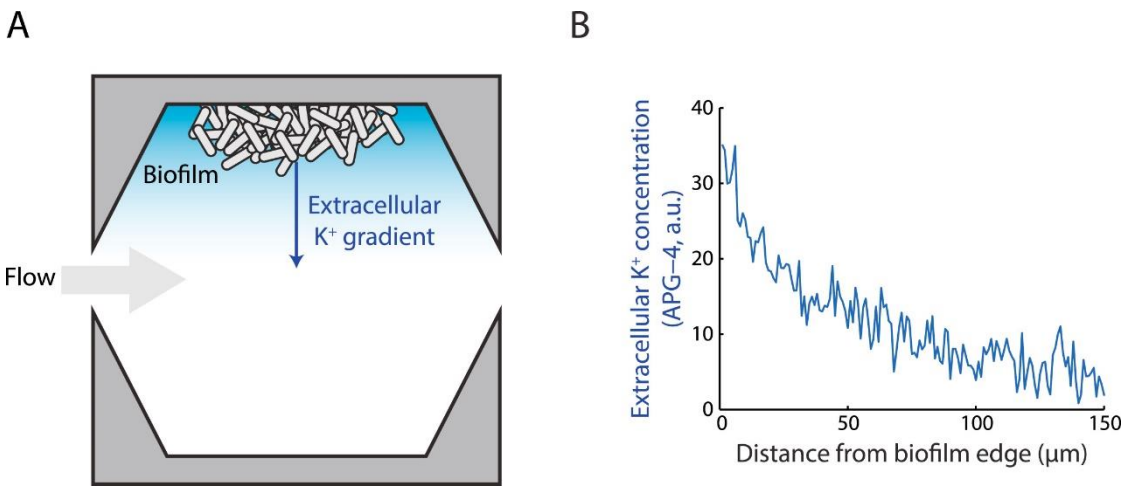

Figure S2.4. a, Illustration of the extracellular potassium gradient (blue shading) formed by biofilms in the microfluidic device. The blue arrow illustrates the biofilm region measured experimentally in (b), and the gray arrow indicates the flow of media relative to biofilm growth and potassium diffusion. **b,** Plot of extracellular potassium produced by the biofilm as a function of distance from the biofilm edge shows a gradient in extracellular potassium. Extracellular potassium is measured with the extracellular potassium specific dye APG-4.

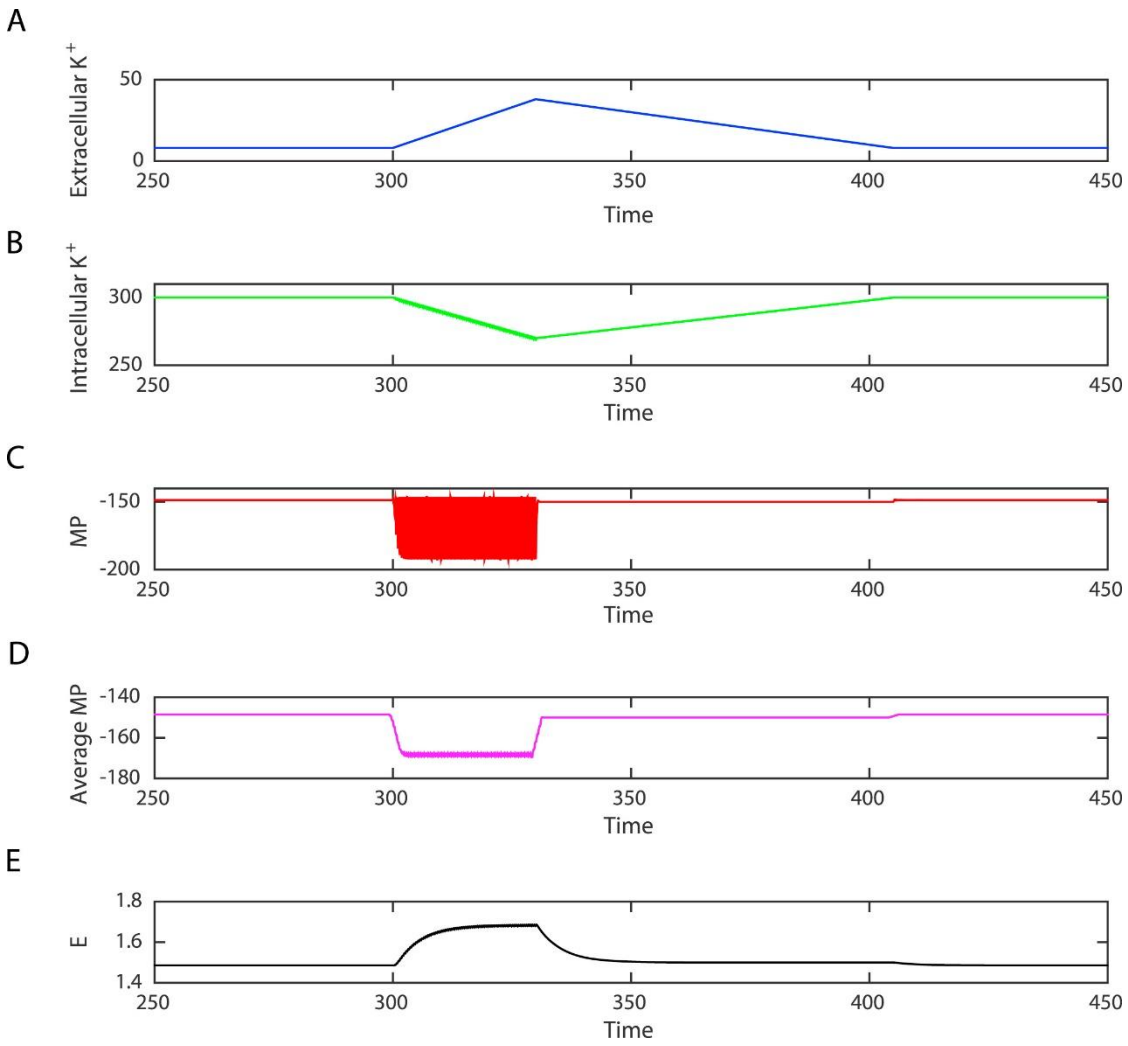

Figure S2.5. a-e, Mathematical modeling of the motile cell response to extracellular potassium released by a biofilm. **a,** Extracellular potassium emitted from the biofilm over time. **b,** Intracellular potassium in motile cells over time. **c,** Instantaneous membrane potential (MP) in motile cells over time. **d,** Average membrane potential in motile cells over time. **e,** Average energy in motile cells over time.

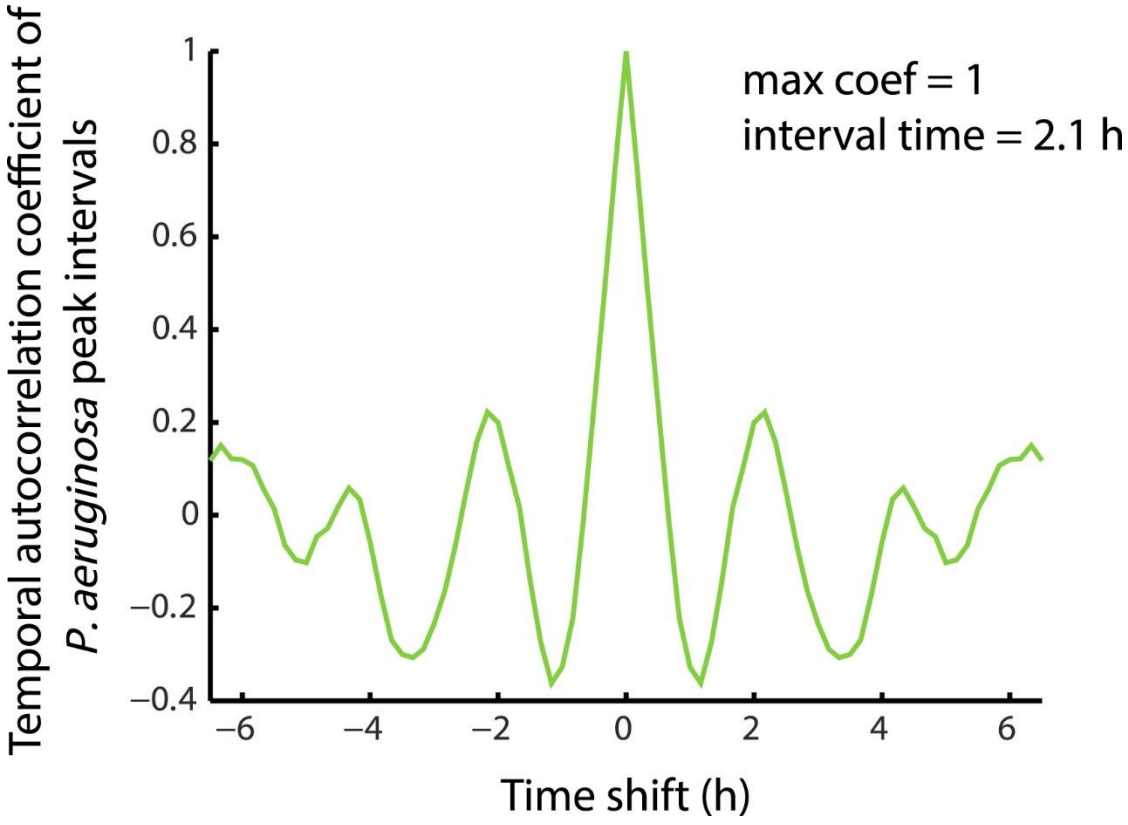

Figure S2.6. Representative temporal autocorrelation coefficient of oscillations in *P. aeruginosa* motile cell attraction shows periodicity and an average peak interval time of 2.1 hours.

Chapter 2.14 - Methods

Bacterial Strains:

All experiments were performed using the *Bacillus subtilis* strain NCIB 3610 and the *Pseudomonas aeruginosa* strain PA01. *B. subtilis* 3610 was a kind gift from W. Winkler (University of Maryland) (Irnov & Winkler 2010). *P. aeruginosa* PA01 was a kind gift from K. Pogliano (University of California, San Diego) and contained a td-Tomato fluorescent reporter plasmid which was made by J. Aguilar (University of California, San Diego). All strains used in this study can be found in Table S1 and were derived from *B. subtilis* 3610 or *P. aeruginosa* PA01. *B. subtilis* motile cells contained an mKate2 reporter under the control of the inducible P_{hyp} promoter (1 mM IPTG was used for induction). In addition, the *sinI* gene (regulator of biofilm formation) was deleted in motile cells in order to reduce clogging in the device. The mKate2 construct was a kind gift from R. Losick. The *ΔtrkA* and *Δhag* strains were made by PCR amplifying 1 kb regions upstream and downstream of the gene to be deleted and cloning them into the pER449 vector (gift from W. Winkler) flanking an antibiotic resistance cassette. Constructs were sequence verified and chromosomally integrated using a standard one-step transformation procedure (Jarmer et al. 2002). The *ΔktrA* strain was made by obtaining the KtrA deletion strain BKE31090 from the Bacillus Genetic Stock Center and using it as a donor to move the *ΔktrA::mls* construct into strain 3610 via SPP1-mediated phage transduction into the 3610 background (Yasbin & Young, 1974). For *ΔktrA* and

Δhag cells, a constitutive reporter was then chromosomally integrated using the one-step transformation procedure. Integrations were confirmed by colony PCR.

Table S2.1. List of strains used in chapter 1

Species and strain	Genotype	Source
B. subtilis		
Wild type	*B. subtilis* NCIB 3610	(W. Winkler) (Irnov & Winkler 2010)
mKate2ΔsinI	3610 *AmyE::P_{hyp}-mKate2*, *sinI::neo*	This study
YFPΔhag	3610 *AmyE::P_{hyp}-YFP, hag::cat*	This study
yugOΔtrkA	*trkA::neo*	(Prindle et al. 2015)
mKate2ΔktrA	*ktrA::mls*	This study
P. aeruginosa		
td-Tomato	*P. aeruginosa* PA01/pJA06-miniRK2 *P_{Spac}-tdTomato::kan*	This study

Growth conditions and dye concentrations:

Biofilms were grown in MSgg medium: 5 mM potassium phosphate buffer (pH 7.0), 100 mM MOPS buffer (pH 7.0, adjusted with NaOH), 2 mM $MgCl_2$, 700 µM $CaCl_2$, 50 µM $MnCl_2$, 100 µM $FeCl_3$, 1 µM $ZnCl_2$, 2 µM thiamine HCl, 0.5% (v/v) glycerol, and 0.5% (w/v) monosodium glutamate. MSgg medium was made fresh from stocks the

day of the experiment. Glutamate and iron stocks were made fresh weekly. ThT (Sigma-Aldrich) was used at a final concentration of 10 µM and APG-4 (TEFLabs) was used at 2 µM. The P_{hyp} reporter used in motile cells was induced using 1 mM IPTG. Biofilms were acclimated for at least 1 hour to any dyes and inducers used in the experiment before addition of motile cells.

Microfluidics and motile cell culturing:

B. subtilis biofilms were grown to a mature state (~20h of growth), and then a separately grown planktonic cell culture of either *B. subtilis* or *P. aeruginosa* was introduced into the growth chamber with the biofilm.

Biofilm growth:

For microfluidic culturing, we used a CellASIC ONIX Microfluidic Platform and Y04D microfluidic plates (EMD Millipore). The day before growing biofilms, the strain to be used was streaked out onto LB agar plates from -80 ^{o}C glycerol stocks. The following day, a single colony was picked from the biofilm strain plate and inoculated in 3 mL lysogeny broth (LB). After 3h of growth shaking at 37 ^{o}C, cells were spun down at 2100 rcf for 1 min, re-suspended in fresh MSgg and loaded into the microfluidic chamber. After loading, cells were incubated at 32.5 ^{o}C overnight, then 30 ^{o}C for the rest of the experiment. Prior to addition of motile cells, biofilms were grown with media supplied at 1.5 psi from one well.

Motile cell growth:

Motile cell strains to be used were streaked out onto LB agar plates from -80 ^{o}C glycerol stocks. The same night as biofilms were initially loaded and growing, a single colony of the *B. subtilis* motile cell strain to be used was inoculated in 3 mL of MSgg + 1 mM IPTG and any fluorescent reporters such as ThT or APG-4 to be used in the experiment. This culture was grown overnight (10-14 h) in a 15 mL culture tube shaking at 37 ^{o}C. In the morning, the culture was re-suspended in fresh MSgg and immediately loaded into the microfluidic chamber. Non-motile *Δhag B. subtilis* cells were cultured and introduced into the microfluidic device in the same manner as motile *B. subtilis* cells. *P. aeruginosa* motile cells were cultured in the same way as *B. subtilis,* except after growth overnight, the culture was diluted 1:30 in fresh MSgg and allowed to grow at 37 ^{o}C shaking for 2 hours before re-suspending in fresh MSgg, and loading into the microfluidic chamber.

After the onset of oscillations in the mature biofilm, motile cells were introduced into the microfluidic chamber. The OD of motile cells was measured and normalized to 1 for *B. subtilis* and 0.5 for *P. aeruginosa*. Motile cells were passed through a 5 μm filter to remove any cell aggregates, spun down at 2100 rcf for 1 min, and resuspended in fresh MSgg + 1 mM IPTG + fluorescent dyes. Motile cells were allowed to flow into the chamber through a dedicated media inlet well. The flow rate (12 μm/sec) was low enough to supply the growth chamber with fresh media while not

being so fast that it prevented motile cells from being able to swim upstream against the flow.

The potassium addition experiment shown in Figure 2 was performed by growing a single biofilm on one side of the growth chamber and introducing an artificial potassium source into the other side of the chamber. In addition to the inlet used to flow in the motile cell suspension, a potassium concentration gradient could be produced by flowing MSgg supplemented with 300 mM KCl from the inlet furthest from the biofilm.

Time-lapse microscopy:

Growth of biofilms was tracked using phase contrast microscopy and motile cell behavior was tracked by fluorescence microscopy of the P_{hyp}-*mKate2* reporter (only present in motile cells). The imaging systems used were Olympus IX83 with an X-Cite LED light source from Lumen Dynamics and Olympus IX81 with a Lambda XL light source from Sutter Instruments. Attraction experiments were acquired using a 10X objective and a 40X objective was used to evaluate ThT intensity in motile cells for the experiments shown in Figure 4c, d and Figure 5d. During time lapse experiments, phase and fluorescence images were taken in 10 minute intervals.

Computational model for electrical attraction

Our agent-based model assumes that each motile cell changes its electrophysiological state and motility independently of each other and only in response to changes in extracellular potassium. We describe intracellular potassium-driven dynamics within each cell using a generalization of the electrophysiological model introduced in our earlier paper (Prindle et al. 2015). The membrane potential is governed by the standard Hodgkin-Huxley-type conductance equation

$$\eta C \frac{dV}{dt} = -g_K n^4 (V - V_K) - g_L (V - V_L) \quad (1)$$

in which *C* is the capacitance of the cell membrane. The first term in the right hand side describes the change in membrane potential by potassium ions escaping the cell through potassium ion channels, while the second term describes the leak current. In the standard Hodgkin-Huxley model, the membrane potential dynamics are very fast (milliseconds), much faster than the slow changes in extracellular potassium and corresponding changes in bacterial motility (hours). Since it is very difficult to simulate together processes of such vastly different time scales, we introduced a scaling factor η to slow down the intracellular electrophysiological dynamics. The scaling factor is also applied to Eq. (3) and (4). As long as the electrophysiological processes remain much faster than the slow part of the model, this did not have an appreciable effect on the slow dynamics of the cellular population. We used the value $\eta = 300$ and verified that changing this factor to 150 did not appreciably affect the results of our simulations.

The resting potentials V_k and V_L are set by the ion pumps, and generally are dependent on both intra- and extracellular potassium levels, for which we assume a simple linear form,

$$V_K = V_{K0} + \delta_K(K_e + K_i); \quad V_L = V_{L0} + \delta_L(K_e + K_i) \tag{2}$$

The fourth power in the first term of (1) stems from the fact (Doyle et al, 1998) that bacterial potassium channels are formed by four subunits, which on average are open during a fraction of time *n* whose dynamics is given by the following rate equation:

$$\eta \frac{dn}{dt} = \alpha(S)(1 - n) - \beta n \tag{3}$$

where the first term describes channel opening and the second term specifies the rate of channel closing. As in Prindle et al. (2015), the opening rate α of the potassium channel is assumed to depend on metabolic stress, *S*, according to the Hill function $\alpha(S) = \frac{\alpha_0 S^m}{S_{th}^m + S^m}$. This metabolic stress variable that stands for the concentration of stress-related metabolic products (Cao et al. 2013), such as excess NAD^+ (Roosild et al. 2002; Schlösser et al. 1993) is itself controlled by the membrane potential according to the equation

$$\eta \frac{dS}{dt} = \frac{\alpha_s(V_{th} - V)}{\exp\left(\frac{V_{th} - V}{\sigma}\right) - 1} - \gamma_s S \tag{4}$$

In departure from our previous model (Prindle et al. 2015) that described time-dependent dynamics of the extracellular potassium in the dense biofilm environment, here we assume that motile cells have sufficiently low density and therefore do not change the extracellular potassium appreciably. Instead, we focus on the concentration of the intracellular potassium K_i,

$$\frac{dK_i}{dt} = -\varepsilon g_K n^4 (V - V_K) + \beta_K (V_0 - V) \quad (5)$$

where the first term describes the flux of potassium through ion channels and the second term describes the action of potassium pumps which maintain the membrane potential at the resting value V_0. The second term only appears when $V_0 > V$ and is zero otherwise, because the ion pump can only pump the potassium from outside to inside of a cell.

It can be shown that the regulation of the intracellular potassium described by Eq. (5) plays the role of the integral feedback control loop similar to other mechanisms of bacterial chemotaxis (Yi et al. 2000). Indeed, in the absence of stress ($S \approx 0$), the ion channels are closed ($n \approx 0$), and the membrane potential equilibrates near $V = V_0$ independently of the level of extracellular potassium (perfect adaptation). However, a change in extracellular potassium levels may cause complex transient changes in the membrane potential. When extracellular potassium level rises, according to Eq. (1) it slightly depolarizes the cell (increases V). The depolarization causes opening of the ion

channels ($n > 0$), intracellular potassium flushes out according to Eq. (5), and the cell becomes strongly hyperpolarized. Then the channels close, and the ion pumps restore the membrane potential to the resting value. If the level of extracellular potassium continues to rise, the process repeats, and a periodic sequence of depolarization pulses ensues (see Fig. S5). If the level of extracellular potassium slowly decreases, it slightly hyperpolarizes the cell, but the channels remain closed, and the ion pump maintains the membrane potential close to the resting value. These transient changes in the membrane potential lead to changes in intracellular energy levels (we can think of this energy as PMF or ATP) and in turn lead to changes in the bacterial motility. We describe the energy dynamics by the simple relaxation equation

$$\frac{dE}{dt} = -\alpha_E V - \gamma_E E \tag{6}$$

and postulate that the tumbling probability is downregulated by the energy:

$$\mathcal{P} = \frac{K_E^q}{(E - E_0)^q + K_E^q} \tag{7}$$

The strong anisotropy in the dynamics of the membrane potential for increasing and decreasing extracellular potassium leads to the chemotactic response of motile bacteria to the spatial gradient of potassium. Indeed, if a cell swims up the gradient, it experiences rising levels of potassium and strongly hyperpolarizes, thus increasing the mean proton motive force and the level of energy in the cell. Therefore, its tumbling

probability diminishes, and the cell continues to swim in the same direction. However, when the cell swims down the potassium gradient, hyperpolarization does not occur, and the tumbling probability remains high.

To simulate bacterial motion, we adapted the mechanical agent-based model developed in our earlier work (Volfson et al. 2008; Mather et al. 2010). Each cell is modeled as a spherocylinder of unit diameter that grows linearly along its axis and divides equally after reaching a critical length $l_d = 4$. It can also move along the plane due to forces and torques produced by interactions with other cells and its own flagellae-mediated motility (however, we do not model the flagella dynamics explicitly). The slightly inelastic cell-cell normal contact forces are computed via the standard spring-dashpot model, and the tangential forces are computed as velocity-dependent friction. During periods of directed motion, the cell experiences a self-propelling force directed along its axis. During the periods of tumbling, the self-propelling directional force is switched off, and the cell experiences a strong random torque which quickly turns it in a random new direction. The probability of switching from directed motion to tumbling for each cell is controlled by variable $\mathcal{P}$ that is computed from the electrophysiological cell model. Biofilm-bound cells were assumed to be non-motile (no self-propelling force, no tumbling torque).

The dynamics of extracellular potassium ion field were implemented via a reaction-diffusion model where the biofilm cells played the role of sources and sinks of potassium periodically,

$$\frac{\partial K_e(\boldsymbol{r})}{\partial t} = \sum_j f(t)\delta\left(\boldsymbol{r} - \boldsymbol{r}_j\right) + D_k \nabla^2 K_e(\boldsymbol{r}) \tag{8}$$

Here K_e is the extracellular potassium concentration and $\boldsymbol{r}_j$ is the location of the j-th cell, $f(t)$ is the periodic function describing periodic excretion (with rate α_k) and absorption (with rate $-\beta_k K_e$) cycles of extracellular potassium by the biofilm cells, and D_k is the potassium diffusion constant.

Each simulated motile "cell" carried a set of equations (1)-(7) describing its membrane potential dynamics in response to the local extracellular potassium concentration. The effect of the motile cells on the extracellular potassium concentration was ignored. The parameters of the model are shown in Table S1.

We performed multiple simulations in a narrow channel of length 100 and width 20 (Fig. 5b). The biofilm consisting of approximately 200 cells was initially grown in the back of the open channel (200 × 20 μm^2), after which 100 motile cells were introduced into the open space of the channel. Of course, this computational domain represents only a small portion of the microfluidic chamber used in experimental studies, so our computational results only can be interpreted on a semi-quantitative level, as a way to reveal and explore the underlying biophysical mechanism of the

potassium-driven chemotaxis. For simplicity, we also neglected growth and division for motile cells and only considered their motion in response to the external potassium changes. We used periodic boundary conditions on the side walls for motile cells: when a motile cell touches the left wall, it disappears and reappears at the right side and *vice versa*. The non-motile biofilm cells were periodically switched between producing and absorbing potassium.

A typical simulation is shown in Supplemental Movie 4. At each time step we computed the average concentration of potassium and the motile cell density near the biofilm edge. The periodic oscillations of cell density are clearly seen, which indicate the chemotactic response of bacteria to the potassium oscillations. The distribution of the proton motive force shifts between the peak and the trough phases (Fig. 5c), in agreement with experimental findings (Fig. 5d).

Parameters of the model

The aim of the computational model is to reproduce the observed phenomenology semi-quantitatively. Since the electrophysiology of bacterial cells is much less studied than of their mammalian counterparts, the parameters of the electrophysiological equations were taken either from the classical literature (Hodgkin and Huxley, 1952) or our earlier model describing potassium signaling in bacteria (Prindle et al, 2015). Some parameters (such as resting membrane potentials) were deduced from direct measurements. Other model parameters that connect

electrophysiology and motility (marked as “fitting”) were chosen by random parameter search within physiologically relevant ranges and then further improved by manual variation to maximize the agreement with experimental observations.

Quantification and Statistical Analysis:

FIJI/ImageJ (Schindelin et al. 2012; Preibisch et al. 2009) and MATLAB (MathWorks Inc. 2012) were used for image analysis. Biofilm growth, motile cell density at the biofilm edge, and ThT/APG-4 intensity were obtained using the MATLAB image analysis toolbox.

Statistical Analysis:

Statistical analysis was performed using MATLAB. P values of < 0.05 were considered to be statistically significant. To determine whether data met assumptions of the statistical tests used, MATLAB’s skewness and kurtosis functions were used. Data sets did not have excessive skew or kurtosis and thus were assumed to be normally distributed.

Motile cell and biofilm ThT measurements:

Phase contrast images were used to determine the coordinates of the biofilm edge. Based on the coordinates of the biofilm edge, a 100 µm wide region was established both inward (towards biofilm interior) and outward from the biofilm edge

(See illustration in Figure 1a). The 100 μm region inside the biofilm was used to measure ThT intensity within the biofilm and the 100 μm region outside the biofilm was used to measure motile cell fluorescent reporter intensity in the region immediately surrounding the biofilm. The average intensities obtained from these regions were reported as the biofilm ThT and motile cell density near biofilm time traces. The motile cell density values were normalized to the density of the cell suspension introduced into the device. ThT traces were detrended using MATLAB's "detrend" function. Specifically, the function fits a least-squares line to the data and subtracts this linear trend from the data.

The motile cell response reported in Figure 3d was obtained by averaging the intensities of motile cell attraction peaks from multiple experiments to obtain a single motile cell response measurement. The biofilm signal average reported in Figure 3d was obtained in a similar way, by averaging the intensities of ThT peaks for multiple experiments into a single maximum biofilm ThT measurement. A similar analysis was done for Figure 7f, g, except the peak intensities of attracted motile cells were averaged for each independent biofilm so that they could be compared to the resulting permanent incorporation of attracted cells for that biofilm. For all these measurements, the exact value of n is presented in the corresponding figure legend and represents the number of independent experiments of each genetic background used.

Motile cell density lag and oscillation period measurements:

The motile cell density lag measurements reported in Figure 1d and Figure 6c were obtained using the peak of motile cell attraction and biofilm ThT. Lag was defined as the time between a biofilm ThT peak and the corresponding peak in motile cell attraction. Positive lag times indicate that a peak in motile cell attraction occurred after a peak in biofilm ThT. For Figure 1d and 6c the exact value of n is presented in the corresponding figure legends and represents the number of peaks of ThT and corresponding attraction shown in the histogram. The period comparisons reported in Figure 1e and Figure 6d were obtained by determining the period, peak-to-peak, of oscillations in biofilm ThT and motile cell attraction. The period of motile cell attraction was then plotted versus the period of the corresponding pulse in biofilm ThT. For Figure 1e and 6d, the exact value of n is presented in the corresponding figure legends and represents the number of periods, peak-to-peak, of oscillations and corresponding attraction included in the plot.

Permanent incorporation of attracted cells:

The permanent incorporation of attracted cells reported in Figure 7f, g was obtained by measuring the average fluorescence intensity of mKate2 (a reporter only present in motile cells) in the 100 μm region immediately inward from the biofilm edge (towards biofilm interior) and normalizing by the area of the evaluated region and the density of the motile cell suspension flowing into the device. Incorporation

measurements were obtained at the conclusion of each experiment. The exact value of n is presented in the corresponding figure legend and represents the number of independent experiments included in each plot.

Membrane potential in motile cells:

Data for Figure 5d was obtained by segmenting motile cells and obtaining ThT fluorescence intensity for each cell using the Oufti software (Paintdakhi et al. 2016) and MATLAB.

Motile cell tracking:

Single cell trajectories for the evaluation of tumbling frequency in motile cells were obtained by analyzing time lapse phase contrast image stacks taken at 10 ms intervals at 40X magnification. The Python based cell tracking software TrackPy and the Anaconda Python platform (Trackpy authors 2016; Continuum Analytics 2016) were used to track single cell movement over time and compile this movement into trajectories for each tracked cell. We included trajectories for cells that were tracked for 500 ms or longer in Figure 4e, f. The exact value of n is presented in the corresponding figure legend and represents the number of motile cell trajectories obtained during the peak and trough of electrical activity. Trajectories obtained with TrackPy were further analyzed using MATLAB. Tumbling events were determined by finding the angle of rotation between each time point of the trajectory and if this

rotational angle was greater than 60 degrees, it was called a tumbling event. Tumbling frequencies are reported as number of tumbling events per second.

Table S2.2. Parameters for the mathematical model.

Parameter	Value	Description	Source
g_K	36 mS/cm^2	potassium ion channel conductance per unit area	(Hodgkin & Huxley 1952)
g_L	0.3 mS/cm^2	leak conductance per unit area	(Hodgkin & Huxley 1952)
C	1 μF/cm^2	membrane capacity per unit area	(Hodgkin & Huxley 1952)
V_{K0}	-688 mV	basal potassium resting potential	measurement
V_{L0}	-5694 mV	basal leak resting potential	measurement
δ_K	1 mV/mM	potassium sensitivity of potassium resting potential	(Prindle et al. 2015)
δ_L	18 mV/mM	potassium sensitivity of leak resting potential	(Prindle et al. 2015)
S_{th}	0.04 mM	metabolic stress constant	(Prindle et al. 2015)
V_{th}	-148 mV	membrane potential threshold	measurement
α_0	0.12 ms^{-1}	maximal opening rate of potassium channel	(Hodgkin & Huxley 1952)
β	0.156 ms^{-1}	potassium channel closing rate	(Hodgkin & Huxley 1952)
m	1	opening rate Hill coefficient	(Prindle et al. 2015)
σ	0.2 mV	steepness of the membrane potential stress response	(Prindle et al. 2015)

Table S2.2, continued. Parameters for the mathematical model.

Parameter	Value	Description	Source
γ_s	0.3 ms^{-1}	stress relaxation rate	fitting
α_s	0.03 mM/(ms mV)	membrane potential stress response rate	fitting
η	300	scaling factor	n/a
ε	7000 (mM cm^2)/(mA min)	rate of potassium flux through the open channel	fitting
β_K	0.8 mM/(min mV)	potassium pumping efficiency	fitting
V_0	-148 mV	pump resting potential	fitting
α_E	0.008 $(min\ mV)^{-1}$	PMF accumulation rate	fitting
γ_E	0.8 min^{-1}	PMF relaxation rate	fitting
E_0	1.535 mM	PMF basal value	fitting
q	7	tumbling rate Hill coefficient	fitting
K_E	0.002 mM	PMF threshold for tumbling rate change	fitting
α_k	64 mM/min	extracellular potassium production rate	fitting
β_k	400 min^{-1}	extracellular potassium consumption rate	fitting
D_k	80000 μm^2/min	extracellular potassium diffusion constant	(Fell & Hutchison 1971)

Chapter 2.15 – Works cited in chapter 2

Abee, T., Hellingwerf, K.J. and Konings, W.N. (1988). Effects of potassium ions on proton motive force in Rhodobacter sphaeroides. Journal of Bacteriology, *170(12)*, 5647–5653.

Continuum Analytics, (2016). Anaconda. Available at: https://www.continuum.io/.

Trackpy Authors, (2016). Trackpy. Available at: http://soft-matter.github.io/trackpy/v0.3.2/#.

Bakker, E.P. and Mangerich, W.E. (1981). Interconversion of components of the bacterial proton motive force by electrogenic potassium transport. Journal of Bacteriology, *147(3)*, 820–826.

Berg, H.C. and Brown, D.A. (1972). Chemotaxis in Escherichia coli analysed by Three-dimensional Tracking. Nature, *239(5374)*, 500–504.

Booth, I.R. (1985). Regulation of cytoplasmic pH in bacteria. Microbiological Reviews, *49(4)*, 359–378.

Brameyer, S., Bode, H.B., and Heermann, R. (2015). Languages and dialects: bacterial communication beyond homoserine lactones. Trends in Microbiology, *23(9),* 521–523.

Cao, Y., Pan, Y., Huang, H., Jin, X., Levin, E.J., Kloss, B., and Zhou, M. (2013). Gating of the TrkH ion channel by its associated RCK protein TrkA. Nature, *496(7445),* 317–322.

Castañeda-García, A., Do, T.T., and Blázquez, J. (2011). The K+ uptake regulator TrkA controls membrane potential, pH homeostasis and multidrug susceptibility in Mycobacterium smegmatis. The Journal of Antimicrobial Chemotherapy, *66(7),* 1489–1498.

Doyle, D.A., Morais Cabral, J., Pfuetzner, R.A., Kuo, A., Gulbis, J.M., Cohen, S.L., Chait, B.T., and MacKinnon, R. (1998). The structure of the potassium channel: molecular basis of K+ conduction and selectivity. Science, *280(5360),* 69–77.

Fell, C.J.D. and Hutchison, H.P. (1971). Diffusion coefficients for sodium and potassium chlorides in water at elevated temperatures. Journal of Chemical & Engineering Data, *16(4)*, 427–429.

Gries, C.M., Bose, J.L., Nuxoll, A.S., Fey P.D., and Bayles, K.W. (2013). The Ktr potassium transport system in *Staphylococcus aureus* and its role in cell physiology, antimicrobial resistance and pathogenesis. Molecular Microbiology, *89(4)*, 760–773.

Hille, B. (2001). Ion Channels of Excitable Membranes 3rd ed., (Massachussetts: Sinauer Associates).

Hodgkin, A.L. and Huxley, A.F. (1952). A quantitative description of membrane current and its application to conduction and excitation in nerve. The Journal of Physiology, *117(4)*, 500–544.

Irnov, I. and Winkler, W.C. (2010). A regulatory RNA required for antitermination of biofilm and capsular polysaccharide operons in Bacillales. Molecular Microbiology, *76(3)*, 559–575.

Jarmer, H., Berka, R., Knudsen, S., and Saxlid, H.H. (2002). Transcriptome analysis documents induced competence of Bacillus subtilis during nitrogen limiting conditions. FEMS Microbiology Letters, *206(2)*, 197–200.

De Jong, M.H., van der Drift, C., and Vogels, G.D. (1976). Proton-motive force and the motile behavior of Bacillus subtilis. Archives of Microbiology, *111(1-2)*, 7–11.

Liu, J., Prindle, A., Humphries, J., Gabalda-Sagarra, M., Asally, M., Lee, D.D., Ly, S., Garcia-Ojalvo, J., and Suel, G.M. (2015). Metabolic co-dependence gives rise to collective oscillations within biofilms. Nature, *523(7562),* 550–554.

Lo, C.-J., Leake, M., Pilizota, T., and Berry, R.M. (2007). Nonequivalence of membrane voltage and ion-gradient as driving forces for the bacterial flagellar motor at low load. Biophysical Journal, *93(1)*, 294–302.

Lundberg, M.E., Becker, E., and Choe, S. (2013). MstX and a Putative Potassium Channel Facilitate Biofilm Formation in Bacillus subtilis A. Driks, ed. PLoS ONE, *8(5)*.

Magnuson, R., Solomon, J., and Grossman, A.D. (1994). Biochemical and genetic characterization of a competence pheromone from B. subtilis. Cell, *77(2)*, 207–216.

Manson, M.D., Tedesco, P., Berg, H.C., Harold, F.M., and Van Der Drift, C. (1977). A protonmotive force drives bacterial flagella. Proceedings of the National Academy of Sciences, *74(7),* 3060–3064.

Mather, W., Mondragon-Palomino, O., Danino, T., Hasty, J., and Tsimring, L. (2010). Streaming instability in growing cell populations. Physical Review Letters, *104(20)*, 208101-1-4.

MathWorks Inc. (2012). MATLAB and Image Processing Toolkit. Available at: https://www.mathworks.com/products/matlab/.

Matsuura, S., Shioi, J., Imae, Y., and Iida, S. (1979). Characterization of the Bacillus subtilis motile system driven by an artificially created proton motive force. Journal of Bacteriology, *140(1),* 28–36.

Meister, M., Caplan, S.R., and Berg, H.C. (1989). Dynamics of a tightly coupled mechanism for flagellar rotation. Bacterial motility, chemiosmotic coupling, protonmotive force. Biophysical Journal, *55(5)*, 905–914.

Meister, M., Lowe, G., and Berg, H.C. (1987). The proton flux through the bacterial flagellar motor. Cell, *49(5)*, 643–650.

Miller, J.B. and Koshland, D.E. (1980). Protonmotive force and bacterial sensing. Journal of Bacteriology, *141(1),* 26–32.

Miller, J.B. and Koshland, D.E. (1977). Sensory electrophysiology of bacteria: relationship of the membrane potential to motility and chemotaxis in Bacillus subtilis. Proceedings of the National Academy of Sciences, *74(11)*, 4752–4756.

Miller, M.B. and Bassler, B.L. (2001). Quorum sensing in bacteria. Annual Review of Microbiology, *55*, 165–199.

Paintdakhi, A., Parry, B., Campos, M., Irnov, I., Elf, J., Surovtsev, I., and Jacobs-Wagner, C. (2016). Oufti: an integrated software package for high-accuracy, high-throughput quantitative microscopy analysis. Molecular Microbiology, *99(4)*, 767–777.

Perego, M., Higgins, C.F., Pearce, S.R., Gallagher, M.P., and Hoch, J.A. (1991). The oligopeptide transport system of Bacillus subtilis plays a role in the initiation of sporulation. Molecular Microbiology, *5(1)*, 173–185.

Plásek, J. and Sigler, K. (1996). Slow fluorescent indicators of membrane potential: a survey of different approaches to probe response analysis. Journal of Photochemistry and Photobiology B: Biology, *33(2)*, 101–124.

Preibisch, S., Saalfeld, S., and Tomancak, P. (2009). Globally optimal stitching of tiled 3D microscopic image acquisitions. Bioinformatics (Oxford, England), *25(11)*, 1463–1465.

Prindle, A., Liu, J., Asally, M., Ly, S., Garcia-Ojalvo, J., and Suel. G.M. (2015). Ion channels enable electrical communication in bacterial communities. Nature, *527(7576)*, 59–63.

Roosild, T.P., Miller, S., Booth, I.R., and Choe, S. (2002). A mechanism of regulating transmembrane potassium flux through a ligand-mediated conformational switch. Cell, *109(6),* 781–791.

Schindelin, J., Arganda-Carreras, I., Frise, E., Kaynigh, V., Longair, M., Pietzsch, T., Preibisch, S., Rueden, C., Saalfeld, S., Schmid, B., Tinevez, J. Y., White, D. J., Hartenstein, V., Eliceiri, K., Tomancak, P., and Cardona, A. (2012). Fiji: an open-source platform for biological-image analysis. Nature Methods, *9(7)*, 676–682.

Schlösser, A., Hamann, A., Bossemeyer, D., Schneider, E., and Bakker, E.P. (1993). NAD+ binding to the Escherichia coli K(+)-uptake protein TrkA and sequence similarity between TrkA and domains of a family of dehydrogenases suggest a role for NAD+ in bacterial transport. Molecular Microbiology, *9(3)*, 533–543.

Shapiro, J.A. (1998). Thinking about bacterial populations as multicellular organisms. Annual Review of Microbiology, *52*, 81–104.

Shioi, J.I., Imae, Y., and Oosawa, F. (1978). Protonmotive force and motility of Bacillus subtilis. Journal of Bacteriology, *133(3)*, 1083–1088.

Shioi, J.I., Matsuura, S., and Imae, Y. (1980). Quantitative measurements of proton motive force and motility in Bacillus subtilis. Journal of Bacteriology, *144(3)*, 891–897.

Volfson, D., Cookson, S., Hasty, J., and Tsimring, L. (2008). Biomechanical ordering of dense cell populations. Proceedings of the National Academy of Sciences, *105(40)*, 15346–15351.

Waters, C.M. and Bassler, B.L. (2005). Quorum sensing: cell-to-cell communication in bacteria. Annual Review of Cell and Developmental Biology, *21*, 319–346.

Yasbin, R.E. and Young, F.E. (1974). Transduction in Bacillus subtilis by bacteriophage SPP1. Journal of Virology, *14(6),* 1343–1348.

Yi, T.-M., Huang, Y., Simon, M.I., and Doyle, J. (2000). Robust perfect adaptation in bacterial chemotaxis through integral feedback control. Proceedings of the National Academy of Sciences, *97(9)*, 4649–4653.

Chapter 2.16 - Acknowledgements

Chapter 2, in full, is a reprint of the material as it appears in Humphries, J., Xiong, L., Liu, J., Prindle, A., Yuan, F., Arjes, H. A., Tsimring, L., and Suel, G. M., Cell, 2017. The dissertation author was the primary author of this paper.

We would like to thank S. Lockless, T. Cagatay, M. Asally, K. Süel, and J. Garcia-Ojalvo for comments during the writing of the manuscript, San Ly for help with strain construction, K. Pogliano and R. Losick for providing bacterial strains, and D.Y. Lee, J. Larkin, and L. Baumgart for helpful discussions. This work was in part supported by the San Diego Center for Systems Biology (NIH P50 GM085764) and the National Science Foundation (MCB-1616755). The following grants to G.M.S. funded this work: the NIH, National Institute of General Medical Sciences (R01 GM121888), the National Science Foundation (MCB-1450867 50867), the Defense Advanced Research Projects Agency HR0011-16-2-0035), and the Howard Hughes Medical Institute-Simons Foundation Faculty Scholars program. J.H. was supported by the UCSD Cellular and Molecular Genetics Training Program through an institutional grant from the National Institute of General Medicine (T32 GM007240). A.P. was supported by a Simons Foundation Fellowship of the Helen Hay Whitney Foundation and holds a

Career Award at the Scientific Interface from the Burroughs Wellcome Fund. L.X. and L.T. were partially supported by ONR grant N00014-16-1-2093.